8-27-2012

Experimental investigation into lunar melt density and compressibility : the role of titanium

Kathleen Vander Kaaden

Kathleen Vander Kaaden
Candidate

Department of Earth and Planetary Sciences
Department

This thesis is approved, and it is acceptable in quality and form for publication:

Approved by the Thesis Committee:

Dr. Carl Agee, Chairperson

Dr. Rhian Jones

Dr. Charles Shearer

EXPERIMENTAL INVESTIGATION INTO LUNAR MELT DENSITY AND COMPRESSIBILITY: THE ROLE OF TITANIUM

by

KATHLEEN E. VANDER KAADEN

**BACHELOR OF SCIENCE, GEOLOGICAL SCIENCES,
SALEM STATE UNIVERSITY, 2010**

THESIS

Submitted in Partial Fulfillment of the
Requirements for the Degree of

**Master of Science
Earth and Planetary Sciences**

The University of New Mexico
Albuquerque, New Mexico

July 2012

ACKNOWLEDGEMENTS

I would first and foremost like to thank my advisor, Dr. Carl Agee, for the motivation behind this project and for his support and funding throughout the duration of this study. I would also like to thank my committee members, Dr. Rhian Jones and Dr. Chip Shearer; without their time and commitment to my success, this project would not have been possible. I am greatly appreciative for the help I received from Mike Spilde during EPMA analyses and training as well as the training and support from all of the students in the high pressure lab including Laura Burkemper, Steve Elardo, and Alison Santos. I am also extremely grateful to Dr. Francis McCubbin who provided me with knowledge needed to succeed not only on this project, but in this field, and support in and out of the lab during the entirety of this work. Lastly, I would like to thank the New Mexico Space Grant Consortium for partial funding of this project.

EXPERIMENTAL INVESTIGATION INTO LUNAR MELT DENSITY AND COMPRESSIBILITY: THE ROLE OF TITANIUM

by

Kathleen E. Vander Kaaden

B.S., Geological Sciences, Salem State University, 2010

M.S., Earth and Planetary Sciences, University of New Mexico, 2012

ABSTRACT

This study focuses on determining the density and compressibility of four lunar picritic glasses as a function of TiO_2 content from 0-11 GPa and 1748-2473 K (1475-2200°C). These glasses are hypothesized to have quenched rapidly as glass beads during lunar fire fountain eruptions. The lunar glass beads have distinctive colors that correspond to TiO_2 content. The glasses of interest for this study are the Apollo 15 green glass Type C (A15C) which has a TiO_2 content of 0.26 wt%, the Apollo 14 yellow glass (A14Y) which has a TiO_2 content of 4.58 wt%, the Apollo 17 orange glass 74220-type (A17O) which has a TiO_2 content of 9.12 wt%, and the Apollo 14 black glass (A14B) which has the highest TiO_2 content with 16.40 wt%. These glasses are believed to represent primary, unfractionated melts making them excellent candidates for experimental studies into lunar basalt density and eruptability during partial melting of the lunar mantle. We performed sink-float experiments on these lunar glass compositions using a piston-cylinder apparatus ($P < 2$ GPa) and Walker-style multi-anvil device ($P > 2$ GPa) in order to bracket the density of these melts. We report new sink-float data for A15C, A14Y, and A17O. We find that with increasing pressure, the melts with less TiO_2

are more compressible than high TiO_2 melts. This causes the melt with the most TiO_2 (A14B) to be the least dense at higher pressures, a complete reversal of what is seen at lower pressures. This change in density and compressibility is attributed to the change from $^{[IV]}Ti^{4+}$ to $^{[VI]}Ti^{4+}$ in the melt structure for melts with high TiO_2 contents. We have identified density crossovers between these melts and their equilibrium olivines and pyroxenes, and show that these glasses, with the exception of A17O, should be able to rise to the surface as a result of buoyancy forces alone. For the eruption of A17O, we must call upon the rising diapir model of Hess (1991) to explain its eruptability.

Table of Contents

List of Figures

List of Tables

1. Introduction

1.1 Lunar Volcanic Glasses

Mare volcanism on the Moon is hypothesized to have lasted about 2 Ga with the two main episodes of concern for this study occurring between 3.6-3.9 Ga (high-Ti basalts) and 3.16-3.4 Ga (low and very-low-Ti basalts) (Shearer et al., 2006). Analysis of the volcanic products brought back from the Apollo missions show that mare volcanics are most likely the product of secondary melting of a highly differentiated mantle source created as a result of crystallization of the lunar magma ocean (LMO) (Delano, 1986; Shearer et al., 2006). The eruption products of concern for this study are the lunar glasses which are believed to be the result of rapid quenching of lunar fire fountains (Delano, 1986). Found amongst mare basalts, lunar picritic glasses are thought to be pristine igneous samples derived directly from the deep lunar interior (Delano, 1986). The term picritic refers to the higher amounts of olivine and pyroxene found among these glasses in comparison to basalts. The glass beads have distinctive colors that correspond to TiO_2 content. For example, Apollo 17 orange glass (A17O) has a high TiO_2 content of 9.12 wt% TiO_2, Apollo 14 yellow glass is low with 4.58 wt%, and Apollo 15 green glass is very low with 0.26 wt% (Delano, 1986). These glasses all have high FeO and MgO contents, low Al_2O_3, CaO, and Na_2O contents, and their melt densities are among the highest found on the terrestrial planets (Circone and Agee, 1996).

Knowledge of the density, compressibility, and other physical properties of magmas at high pressure is required in order to understand the differentiation of planetary interiors. Since the lunar glasses are thought to be the most primitive material from the Moon, determining if there is a direct correlation between TiO_2 content with density and compressibility will aid in the constantly improving physical models of lunar

differentiation (Murthy et al., 1971; Longhi, 1980; Warren, 1992). Some fundamental questions lunar scientists have been asking since the Apollo era include: What are the densities of the Moon's magmatic materials? How have these materials erupted to the surface and formed glass beads? Does the vast difference in TiO_2 content of the lunar glasses have any effect on density and compressibility of the melts? Through the experimental study discussed in this paper, we have been able to make profound advances towards answering these questions.

The glasses of concern for this study are the Apollo 15 green glass C (A15C), Apollo 14 yellow glass (A14Y), and the Apollo 17 orange glass (74220-type) (A17O) ranging in wt% TiO_2 from 0.26 to 9.12 (Table 1). We have also reexamined the Apollo 14 black glass (A14B) which has been previously studied by Circone and Agee (1996). The lunar picritic glasses are thought to be pristine igneous samples produced by rapid quenching of lunar fire fountains (Ridley et al., 1973; Heiken et al., 1975; Delano, 1979 & 1986; Elkins-Tanton et al., 2003b). The high Mg#'s of these glasses (Table 1) show they are mainly primary, unfractionated melts since Mg#'s decrease with increasing crystallization, making these glasses a prime candidate to experimentally study lunar basalt petrogenesis (Smith and Agee, 1997).

The goal of this study is to experimentally determine the effect of TiO_2 on lunar magma density and compressibility for the orange, yellow, and green Apollo glasses through sink-float experiments from 0-11 GPa. As part of this work, we have developed a new technique to determine equilibrium olivine and pyroxene compositions through use of the Ulmer (1989), Toplis (2005), and QUILF (Anderson et al., 1993) models. Our data enable us to identify density crossovers that may occur within the lunar mantle. We also

discuss the change in coordination from $^{[IV]}Ti^{4+}$ to $^{[VI]}Ti^{4+}$ and its role in lunar magma density and compressibility, as well as the eruptability of each of these glasses.

Table 1. *Lunar glass compositions.* This table gives the composition of the lunar glasses that we focused on in this study.

	SiO_2	TiO_2	Al_2O_3	Cr_2O	FeO	MnO	MgO	CaO	Na_2O	K_2O	Mg #
Apollo 15 Green C Glass[a]	48.00	0.26	7.74	0.57	16.50	0.19	18.20	8.57	n.d.	n.d.	66.30
Synthetic A15C[b]	47.28	0.29	8.79	0.56	16.29	0.25	18.43	7.87	0.13	0.10	66.90
Apollo 14 Yellow Glass[a]	40.80	4.58	6.16	0.41	24.70	0.30	14.80	7.74	0.42	0.10	51.60
Synthetic A14Y[b]	41.34	4.54	6.60	0.36	24.47	0.33	14.51	7.20	0.05	0.15	51.40
Apollo 17,74220 Orange Glass[a]	38.50	9.12	5.74	0.69	22.90	n.a.	14.90	7.40	0.38	n.d.	53.70
Synthetic A17[c]	38.90	8.87	5.81	0.67	22.30	0.27	15.70	7.37	0.26	-------	55.70
Apollo 14 Black Glass[a]	34.00	16.40	4.60	0.92	24.50	0.31	13.30	6.90	0.23	0.16	49.20

[a]Delano (1986), [b]This study, [c]van Kan Parker et al. (2011)

1.2 Magma Ocean Differentiation

The concept of a lunar magma ocean (LMO) was proposed in the early 1970s, once samples had been brought back and analyses were underway from Apollo 11 (Wood et al., 1970; Smith et al., 1970). In order for an LMO to exist, there must have been a major heating event that melted a majority of the Moon. Many possible heat sources have been suggested, including the decay of short-lived radioactive species, heat inherited from the Earth (fission hypothesis), increased solar luminosity, and rapid accretion of the planetary body (Warren, 1985; Shearer et al., 2006). Rapid accretion seems to be the most feasible heat source for producing the amount of melting required for a LMO as it is in agreement with the generally accepted giant impact hypothesis for lunar formation. Models predict that the debris orbiting the Earth after the giant impact would have accreted very rapidly, melting a substantial portion of the Moon (Shearer et al., 2006). As the LMO began to cool, the dense olivine and pyroxene that crystallized out would have sunk to the bottom of the magma ocean as a result of their high density relative to the melt, forming a cumulate pile. The plagioclase that crystallized from the remaining liquid

would have been buoyant and floated to the top, creating a stratigraphically diverse LMO. Olivine, pyroxene, and plagioclase continued to crystallize causing the melt to become enriched in TiO_2. This hypothesis accounts for the thick (~60 km) anorthositic crust and ultramafic mantle found on the Moon today (Wieczorek et al., 2006).

In order to form the suites of rocks we see on the Moon, it is hypothesized that as crystallization of the LMO continued, the cumulate pile was overturned due to gravitational instabilities (Hess and Parmentier, 1993). This solid state overturn resulted in titanium-rich cumulates sinking to the bottom of the LMO while the olivine and pyroxene cumulates began to rise. As the cumulate pile was remelted the magma became even more differentiated (Grove and Krawczynski, 2009). The product of this remelting can be seen in the compositionally diverse mare basalts and ultramafic glasses (Grove and Krawczynski, 2009).

1.3 Previous Studies on Lunar Melt Density

Sink/float experiments have previously been carried out on compositions equivalent to Apollo 14 black glass, Apollo 17 orange glass and Apollo 15 green glass from 0.5-12 GPa, 0.8-8.5 GPa, and 0.5-3.5 GPa, respectively (Circone and Agee, 1996; van Kan Parker et al., 2011; Smith and Agee, 1997). The sink/float method is an experimental technique in which the starting material of concern is packed into a capsule with a sphere of known density placed at the top and bottom (Agee and Walker, 1988). This method is used to determine the density of the melt relative to two density markers at target pressure and temperature. Sinking spheres are interpreted as being more dense than the melt and floating spheres as less dense (Figure 1A&B). If there is no movement

of the spheres observed this is interpreted as a neutral buoyancy, signifying the density of the spheres is equivalent to that of the melt (Figure 1C).

Prior to this study, the densest melt of all the compositions investigated was the Apollo 14 black glass (A14B) with 16.4 wt% TiO_2 and 24.5 wt% FeO. Its calculated 1-bar liquidus density of ~3.13 g/cm^3 led Delano (1986) to predict that this melt would be negatively buoyant relative to coexisting liquidus olivines and pyroxenes at a depth of approximately 500 km in the lunar mantle. Lunar magmas with higher TiO_2 contents than A14B may be absent from the lunar surface because they were too dense to rise from their mantle source regions. Some researchers have even argued for an Fe-Ti oxide rich lunar core (de Vries et al., 2011). Circone and Agee (1996) carried out high pressure sink/float density measurements on molten black glass and confirmed Delano's original idea. They found that molten black glass was the most compressible mantle silicate melt yet studied and that it would be negatively buoyant relative to an olivine-pyroxene source rock at depths >400 km. Thus, fire fountain eruptions of A14B magma are an enigma, because they should not rise to the surface. We have investigated this conundrum in our study and discuss a solution to it in section 4.3.

Sink/float experiments were performed by van Kan Parker et al. (2011) on a synthetic composition of the orange glass with 8.78 wt% TiO_2 and 22.3 wt% FeO. The calculated 1-bar density of the orange glass has not yet been definitively determined with possibilities at 3.02 g/cm^3, 3.01 g/cm^3, and 2.99 g/cm^3 (Delano, 1990; Lange and Carmichael, 1987; Ghiorso and Kress, 2004). These experiments indicate a density crossover between molten orange glass and equilibrium orthopyroxene at about 600 km depth in the lunar mantle (~2.8 GPa). Since this depth is slightly deeper than the multiple

saturation point of the orange glass, its eruption to the surface is not hindered. A density crossover with equilibrium olivine is predicted to occur at pressures greater than 4.7 GPa which falls outside the lunar pressure range. Although experiments were completed up to 8.5 GPa, many data points at higher pressure gave ambiguous results. In our study, we performed more experiments in the range of 6-12 GPa in order to make a full comparison with the black glass.

Smith and Agee (1997) carried out four experiments on A15C green glass at 0.5, 2.5, 3, and 3.5 GPa. A15C contains 0.26 wt% TiO_2 and 16.5 wt% FeO and has a calculated 1-bar liquidus density of ~2.82 g/cm^3. It is predicted to have a density crossover with equilibrium pyroxene at a depth of about 800 km (3.5 GPa). These experiments also predict A15C to be less dense than equilibrium olivine over the range of pressures applicable to the lunar interior (Smith and Agee, 1997). In our study we included more experiments in the range of 3.5-12 GPa for A15C, in order to better constrain the density and compressibility of this composition and to make a full comparison with the other previously studied lunar volcanic glasses mentioned above.

2. Methods

2.1 Starting Material

The synthetic starting material for the orange glass was made at MIT by Mike Krawcynzki: details are given in van Kan Parker et al. (2011). The synthetic starting material for the green and yellow glasses was made at the University of New Mexico (UNM). High purity reagent grade powdered oxides and silicates were combined and ground under ethanol using an agate mortar and pestle. In order to maintain homogeneity within the mix, reagents were added in multiple steps. First, the smallest amounts of

reagents needed were mixed together for approximately 15 minutes. Additional reagents were added that contained approximately the same volume of powder that had already been mixed. Each addition was ground under ethanol for an additional 30 minutes. The process was continued until all oxides were added and a final mixing time of at least 60 minutes was reached. The synthetic powder was scraped from the mortar and pestle and put into a glass vial. The vial was placed in an oven (~373 K/100°C) to dry off any excess ethanol and/or water that may have accumulated in the mix during the weighing process. For these mixes, Fe was added in the form of Fe^{2+} in fayalite to minimize the reaction between the iron in the mix and the molybdenum from the capsule during the experiments. One to two super-liquidus experiments were run on each synthetic composition to check that homogeneity was maintained throughout the mixing process.

2.2 Experimental

Experiments were conducted using the sink-float technique to create a full compression curve for the orange, yellow, and green Apollo glasses (Agee and Walker, 1988). This method has been used in the past to successfully bracket the density of silicate liquids at high pressures (Agee and Walker, 1993; Knoche and Luth, 1996; Circone and Agee, 1996; Smith and Agee, 1997; Agee, 1998; Suzuki et al., 1998). All experiments were conducted in the high pressure laboratory at UNM. Experiments in the pressure range of 0.5-2 GPa were run using a Depths of the Earth Quickpress™ type piston cylinder (PC). A Walker style multi anvil (MA) device was used for pressures greater than 2 GPa up to 11 GPa. All density markers used were spherical crystals with a diameter of 300-700 μm created in a Bond Air Mill. For the lower pressure experiments

(0.5-4 GPa), forsterite-rich olivine spheres were used whereas pyrope-rich garnets spheres were generally used for experiments above 4 GPa.

For both techniques each experiment is set up by packing the starting material into a molybdenum metal (Mo^0) capsule and placing two mineral spheres, which serve as density markers, at the top and bottom of the capsule. For the PC runs, salt cells were used to ensure anhydrous conditions throughout the runs. For this setup, a graphite heater is surrounded by a pyrex tube and a salt cell. The salt cell is created by compressing 2.5 grams of salt at 83 bars for 45 seconds in the PC. Two MgO spacers are placed at the top and bottom of the cell with the capsule and surrounding MgO sheath in the center (schematic shown in Figure A-1). Following this, Type C ($W_{95}Re_5/W_{74}Re_{26}$) thermocouple wires, are inserted axially below the capsule to record the temperature throughout the run. A steel base plug is inserted around the thermocouple to ensure conductivity throughout the cell. Finally an insulating disk is placed around the steel base plug to make sure that the circuit remains within the cell setup only.

With the MA technique, a ceramic octahedron is constructed with a rhenium heater and Type C ($W_{95}Re_5/W_{74}Re_{26}$) thermocouple wires, located on the center of the outer surface of the heater. Two Al_2O_3 spacers are placed in the heater with an aluminum sheath surrounding the Mo^0 capsule so it sits directly in the center of the octahedron (schematic shown in Figure A-2). The octahedron is surrounded with 8 tungsten carbide cubes, each with a truncation-edge-length of 8 mm, and placed in the hat-box of the MA. For both the PC and MA techniques, the sample is pressurized and rapidly heated at 200-300 K per minute to super-liquidus temperatures (approximately 1720-2423 K depending on desired pressure). The experiments are held at the elevated P-T conditions for at least

30 seconds to allow the synthetic powder adequate time to melt and for the spheres to be driven up or down in the capsule by buoyancy forces. Experiments are limited to these short run durations to prevent dissolution of the spheres into the melt, which would drive the melt composition from the target composition being investigated. The sample is quenched by shutting off the power to the furnace and allowing the run to decompress gradually. The average rate of cooling is approximately 150°/s.

The run products are set in one-inch diameter mounts using Petropoxy and allowed to harden over night. They are ground using various grit sizes of sand paper (240, 320, 400, and 600 equivalent to 53.5 µm, 36 µm, 23.6 µm, and 16 µm, respectively) and polished down to 0.3 µm to reveal the final location of the spheres. The result of each experiment does not provide a direct measurement of the density of the liquid at the experimental conditions but rather gives an open ended bracket on the density. Figure 1A shows an example where the spheres sank, indicating they are more dense than the melt whereas Figure 1B shows floating spheres which are inferred to be less dense than the melt. However, if there is no movement of the spheres observed this is interpreted as a neutral buoyancy (Figure 1C) signifying the density of the spheres is equivalent to that of the melt. Nevertheless, these experiments are typically repeated with slightly longer run durations (45-60 seconds) to ensure that sluggish kinetics were not a problem. The precise density of the liquid is best defined by a neutral buoyancy bracketed by a sink and float at slightly lower and higher pressures, respectively.

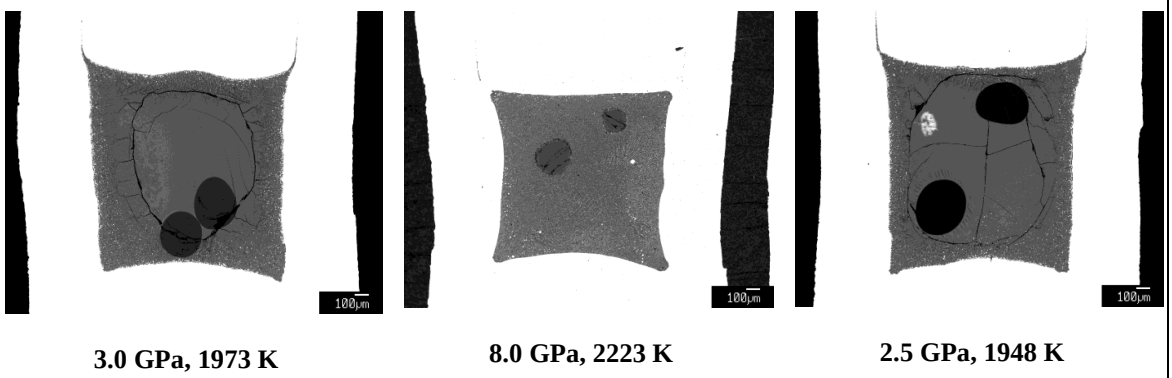

Figure 1. *BSE images of possible results from sink-float experiments.* **A.** YG-KV-15; Dark spheres are Fo_{83}. Represents a sink **B.** OG-KV-5; Dark spheres are Pyrope-rich garnets. Represents a float. **C.** YG-KV-20; Dark spheres are $Fo_{90.}$ Represents a neutral buoyancy.

2.3 Analytical

Polished run products were carbon coated and analyzed by electron probe microanalysis (EPMA) at UNM using a JEOL 8200 Electron Probe Microanalyzer. Samples were analyzed using an accelerating voltage of 15 KeV and a beam current of 20 nA. A broad beam (10-20 µm) was used for glass analyses whereas a focused beam was used for analyses of the mineral density markers. The melt was analyzed to determine the composition and if there were any melt/capsule or melt/sphere interactions. The spheres were analyzed around the center to confirm composition and near the edges to ensure there was no sphere/melt interaction. Standards used for calibration included albite (Na), almandine (Al, Fe), augite (Si, Al, Ca, Mg), olivine (Mg, Si, Fe), orthoclase (K), pyrope (Cr, Mg, Ca), sphene (Ti), and spessartine (Mn). A molybdenum standard ($CaMo_4$) was used to determine the amount of MoO_2 contamination in the glasses for all runs and a sodalite standard was used to determine any Cl contamination in PC runs. Peak and background count times were 20 seconds and 10 seconds, respectively for major elements and 30 seconds and 15 seconds for minor elements.

2.4 Density of Spheres

A well-defined equation of state is needed to determine the density of the spheres at the experimental pressure and temperature conditions, parameters for which are given in Table 2. The densities of the mineral markers in each experiment (olivine and garnet) were calculated using the Birch Murnaghan equations of state:

$$P = \frac{3}{2}K_T\left[\left(\frac{\rho_{T,P}}{\rho_{T,0}}\right)^{7/3} - \left(\frac{\rho_{T,P}}{\rho_{T,0}}\right)^{5/3}\right] * \left[1 - \frac{3}{4}(4 - K')\left(\left(\frac{\rho_{T,P}}{\rho_{T,0}}\right)^{2/3} - 1\right)\right] \quad (1)$$

where K_T is the isothermal bulk modulus defined as:

$$K_T = K_{298} + dK/dT(T - 298) \quad (2)$$

For these equations, K_T is in GPa and T is in Kelvin. In equation (1) P is pressure, K′ is the pressure derivative, and $\rho_{T,0}$ and $\rho_{T,P}$ are the densities of the spheres at temperature T and ambient pressure (10^5 Pa) and high pressure, respectively. The density at 10^5 Pa is given by:

$$\rho_{T,0} = \rho_{298}(T) \exp \int_{298}^{T} \alpha(T)dT \quad (3)$$

in which α is the thermal expansion and defined as:

$$\alpha(T) = \alpha_0 + \alpha_1 T + \frac{\alpha_2}{T^2} \quad (4)$$

The main uncertainty of the sink/float method is the calculation of sphere density through use of these equations which is estimated at ±0.03 g/cm^3 (Circone and Agee, 1996). Some experiments were run at pressure and temperature (PT) conditions that have yet to be defined by equations of state, so this produced an added uncertainty into the study.

Table 2. *Equation of state parameters for calculating sphere density at experimental PT.* Adapted from Circone and Agee (1996) and van Kan Parker et al. (2011).

	K_{298}	dK/dT	K′	α_0	α_1	α_2	P_{298}
Mg_2SiO_4	127.5[a]	-0.02[b]	4.8[a]	3.034E-05	7.422E-09	-5.381E-01[c]	3.229 X_{Fo}[h]
Fe_2SiO_4	134.6[d]	-0.024[d]	5.2[e]	0.2386E-05	11.53E-09	-0.518E-01[f,g,h]	4.417 X_{Fa}[h]
$Ca_3Al_2Si_3O_{12}$	165.68[i]	-0.024[j]	5.46[i]	1.951E-05	8.089E-09	-4.972E-01[k]	3.593 X_{Gr}[p]
$Mg_3Al_2Si_3O_{12}$	171.32[i]	-0.0258[j]	3.22[i]	2.311E-05	5.956E-09	-4.538E-01[k]	3.559 X_{Py}[p]
$Fe_3Al_2Si_3O_{12}$	185[l]	-0.0268[j]	4.2[l]	1.776E-05	12.14E-09	-5.071E-01[k]	4.319 X_{Al}[p]
$MgSiO_3$	95.8[m]	-0.0274[n]	14.9[m]	2.947E-05	2.694E-09	-0.5588[k]	3.206 X_{En}[q]
$FeSiO_3$	95.1[o]	-0.0237[n]	10.6[o]	2.75E-05[n]			4.066 X_{Fs}[q]
Al_2O_3[r]	254.34	-0.02530	4.23	2.71E-05	1.370E-09	-1.1965E+00	3.982

[a] Jacobs and De Jong (2007), [b] Liu and Li (2006), [c] Suzuki(1975), [d] Graham et al. (1988), [e] Isaak et al. (1993), [f] Suzuki et al. (1981), [g] Smyth (1975), [h] Hazen (1977), [i] Conrad et al. (1999), [j] Sumino and Anderson (1984), [k] Skinner (1966), [l] Zhang et al. (1999), [m] Hugh-Jones and Angel (1994) –valid up to 4 GPa, [n] Calculated from Hugh-Jones (1997), [o] Hugh-Jones and Angel (1997), [p] Skinner (1956), [q] Goto et al. (1989).

2.5 Calculation of Density Crossovers

Previous discussion of melt density, authors have reported single compositions of equilibrium olivines or pyroxenes over the entire pressure range of the Moon (Circone and Agee, 1996; Smith and Agee, 1997; van Kan Parker et al., 2011). These authors calculated the Fe-Mg crystal liquid distribution coefficient for both equilibrium olivines and pyroxenes using the following equation:

$$K_D = \frac{(X_{Fe}^S)(X_{Mg}^L)}{(X_{Mg}^S)(X_{Fe}^L)} \quad (5)$$

where K_D is the distribution coefficient, X_i^S is the mole fraction of element i in the solid and X_i^L is the mole fraction of element i in the liquid. Equation (6), adapted from Delano (1990), was then used to determine the effect of TiO_2 on the K_D values.

$$K_D = 0.33 - 0.0071\ (mol\%\ TiO_2\ in\ melt) \quad (6)$$

Previous authors also used equation (7), adapted from Jones (1988), to determine the effect of pressure on K_D.

$$K_D = 0.320 + 0.120\,X_{Mg} + 0.106\,X_{Fe} - 0.863\,X_{Ti} - 0.00007P \quad (7)$$

where P is pressure in GPa.

However, the composition of the equilibrium olivine and pyroxene will change as a function of pressure (Toplis, 2005; Ulmer, 1989; Anderson et al., 1993). Consequently, we find it more realistic to calculate density curves of the minerals in equilibrium with the various melts at pressures relevant to the lunar interior (0-4.7 GPa). To do this, we used two models; that of Toplis (2005) which takes into account mainly the effect of liquid composition on equilibrium olivines and that of Ulmer (1989) which takes into account the effect of pressure on equilibrium olivines. K_D values were calculated using the two models and equilibrium olivine contents were determined. Equilibrium pyroxene compositions were calculated using the program QUILF (Anderson et al., 1993). This procedure was used at both 2173 K (1900°C) as a reference temperature and the temperature of the multiple saturation point (MSP) for each composition. The MSP occurs when two minerals, in this case olivine and pyroxene, coexist on the liquidus. Densities of the equilibrium mineral assemblages were calculated using the 3rd order Birch-Murnaghan EOS (Eq. (1)) and plotted against the experimental data in order to determine where density crossovers occur between each melt and its equilibrium mineral assemblages. For a full discussion on the calculations and procedures for determining density crossovers between equilibrium minerals and their corresponding melt compositions refer to Appendix A.

3. Results

3.1 Green Glass

Appendix B contains experimental run conditions for every experiment used in this study as well as BSE images of each experimental charge. Experimental results for the Apollo 15 green glass (A15C) are summarized in (Appendix) Table B-1 and Figure 2. Experimental charges are shown in (Appendix) Figure B-4. Smith and Agee (1997) experimentally determined the density of A15C up to 3.5 GPa. As discussed in Appendix B, we were unable to reproduce their data due to the optical similarity between the melt and the density markers. However, we report four additional experiments at higher pressure which place better constraints on the density of this melt. We report two sinks and a float of garnet spheres with a composition of $Py_{49}Al_{31}Gr_{18}Sp_1$ at 7 GPa, 7.5 GPa, and 9 GPa with temperatures of 2323 K (2050°C), 2373 K (2100°C), and 2473 K (2200°C), respectively. To place tighter constraints on this density bracket, we also observed the sinking of a garnet sphere with a composition of $Py_{63}Al_{24}Gr_{12}Sp_1$ at 8.5 GPa and 2448 K (2175°C).

For each composition studied throughout this project, the temperature of the experimental run changed as a result of the pressure of interest. However, as the 3rd order Birch-Murnaghan EOS is an isothermal parameter, each density bracketing point had to be corrected to the particular temperature of interest for the specific lunar glass. For each composition, data were corrected using the following example procedure. For A15C, the temperatures of interest for this composition are 2173 K (1900°C) (Figure 2), in order to make a direct comparison with the other glasses at a common temperature, and 1793 K (1520°C) (Figure 3) which is the multiple saturation point (MSP) temperature for this

composition as determined by Wagner and Grove (1997). Data were corrected to 2173 K (1900°C) and 1793 K (1520°C) by first taking the difference between the 1 bar density of our experimental charge at the PT conditions of the run and the 1 bar density of the ideal composition (from Delano, 1986) at 2173 K (1900°C) and 1793 K (1520°C), respectively. We then fixed the density of each data point for this composition by this difference, assuming the shape of the density curve would be the same regardless of temperature, just shifted either up or down. We used the same procedure to correct for compositional differences between the ideal composition of the glass from Delano (1986) and the actual composition of the melt during the run as determined from EPMA.

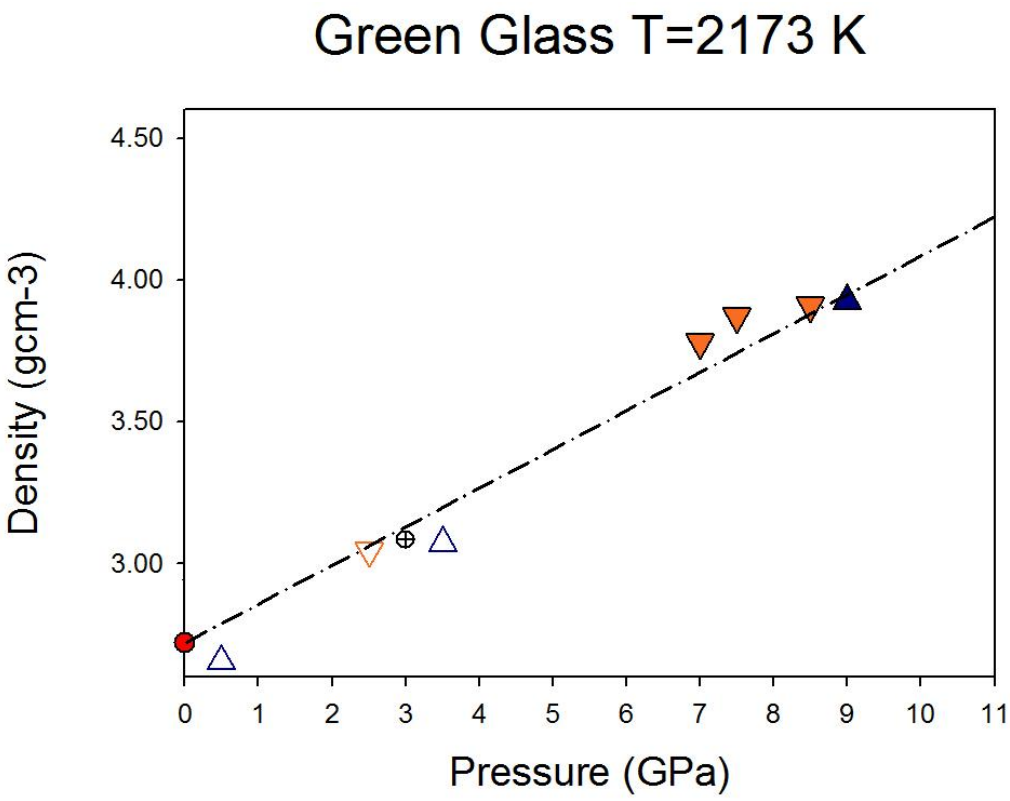

Figure 2. *Experimental results for green glass at T=2173 K (1900°C).* The calculated 1-bar density for this composition at 1900°C (red circle) is 2.72 g/cm^3 (Lange and Carmichael, 1987; Ochs and Lange, 1999). Downward pointing orange triangles represent sinks, upward pointing blue triangles represent floats, and circles represent neutral buoyancy points. Filled data points are from this study and open data points are from Smith and Agee (1997). The dotted line represents the best fit linear line to all available the data.

Data corrected to 1520°C, the MSP, are displayed in Figure 3. In this Figure we have also plotted the densities of equilibrium pyroxene and olivine compositions calculated from Toplis (2005) and Ulmer (1989) discussed in Appendix A. The results of the two models are strikingly similar over the pressure ranges relevant to the lunar interior and can therefore be considered as one set of equilibrium pyroxenes and one set of equilibrium olivines. We attempted to fit a 3rd order BM EOS best-fit line to the current data to estimate melt density; however if we attempt to do so, the value of K′ ends up being less than 4, causing the best-fit line to become convex instead of concave. Hence the density increases towards infinity at a single pressure which we know is unrealistic. Therefore, we have fitted a straight line to all of the current experimental density data available. This linear line has an average slope of 0.14 g/cm^3/GPa (Table 3). When we compare the density of this melt with its equilibrium mineral assemblages', we find there is a density crossover with the equilibrium pyroxenes at ~3.75 GPa and a second density crossover with the equilibrium olivines at ~ 3.8 GPa. However, as the MSP for the A15C composition is at 1.3 GPa, both density crossovers between the melt and its equilibrium minerals occur at pressures greater than the MSP. Implications of these results are discussed further in section 4.3 that follows.

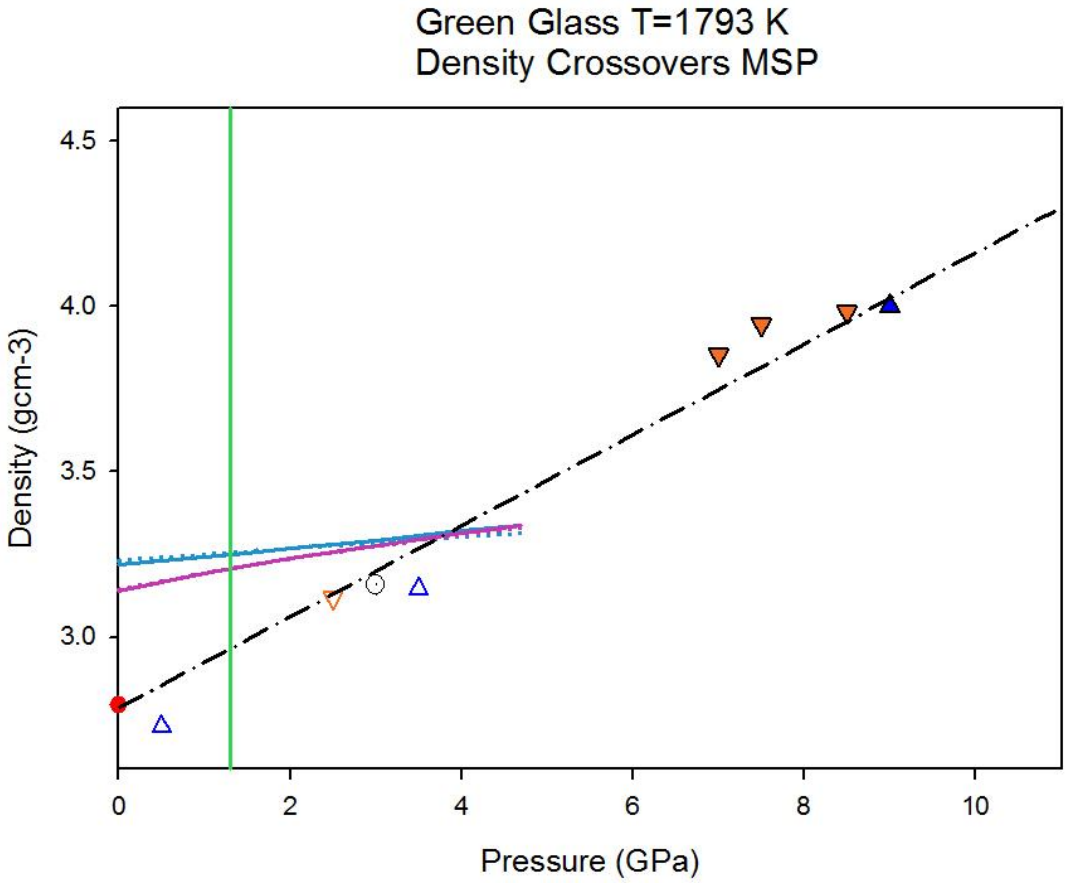

Figure 3. *Experimental results and density crossovers for green glass at T=1793 K (1520°C).* The calculated 1-bar density for this composition (red circle) at 1520°C is 2.79 gcm^{-3} (Lange and Carmichael, 1987; Ochs and Lange, 1999). Symbols are the same as Figure 2. The pink lines show the densities of equilibrium pyroxenes for this composition and the blue lines show the densities of equilibrium olivines. The solid lines are from Ulmer (1989) and the dotted lines are from Toplis (2005). The green solid line shows the MSP at 1.3 GPa.

As discussed in Appendix B, it is difficult to determine the correct liquidus temperature at a given pressure when there is not a fully characterized phase diagram for a particular composition. Because of this, the superliquidus temperature for a given run is sometimes underestimated, resulting in the presence of near-liquidus minerals at the end of a run. However, as long as the spheres move during the run, we can still use these charges where near-liquidus minerals are present. A compositional correction needs to be made for the difference in the composition of the melt that the spheres floated or sank in and the starting composition of the melt. This is done using the same procedure discussed

above for making temperature corrections. For the green glass, we ran four experimental charges where near-liquidus garnets were present at the end of the run (Table B-5). Garnets were present at 9 GPa and temperatures of 2423 K (2150°C) and 2473 K (2200°C), as well as 8.5 GPa and 2448 K (2175°C), and 7.5 GPa and a temperature of 2373 K (2100°C). The compositions of these garnets are $Py_{75}Al_{13}Gr_{11}Sp_{1,}$ $Py_{76}Al_{13}Gr_{10}Sp_{1,}$ $Py_{75}Al_{13}Gr_{11}Sp_{1,}$ and $Py_{74}Al_{15}Gr_{11}Sp_{1,}$ respectively (Table B-5). Using these new data, we are able to extrapolate the phase diagrams from Elkins-Tanton et al. (2003a) and Draper et al. (2006) and almost double the pressure range of the liquidus for this composition (Figure 4).

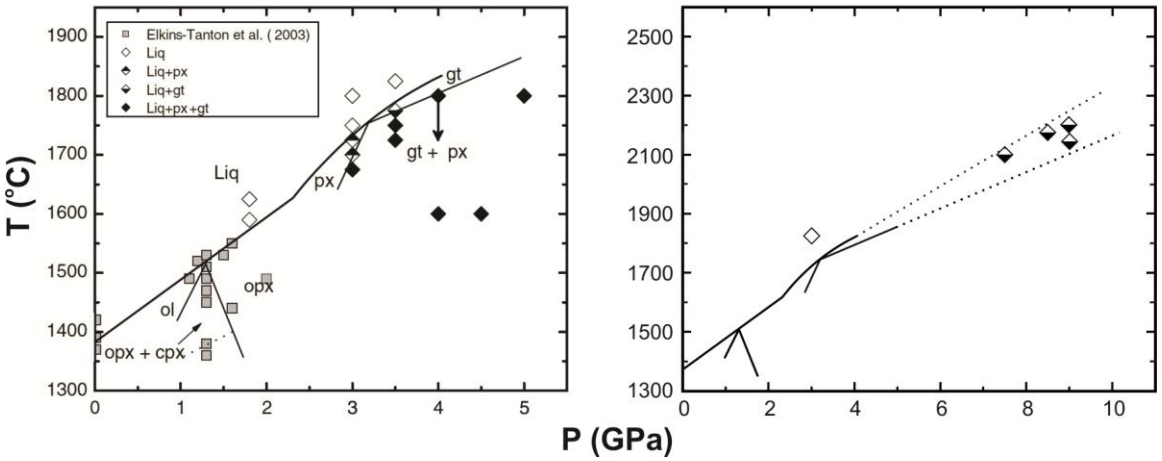

Figure 4. *Phase diagram for A15C.* Using the experimental results from this study we have extrapolated the previous phase diagram for A15C up to 9 GPa and included another data point at 3 GPa. Diagram on the left is from Draper et al. (2006). Symbols are the same in both diagrams.

3.2 Yellow Glass

Experimental results for this composition (A14Y) are summarized in Table B-2 and Figure 5. Experimental charges are shown in Figure B-5. There have not been any data reported on the density of A14Y to date. We present 11 new experimental sink-float results for this composition. Fo_{100} spheres sank in this composition at 1 GPa and 1.5 GPa at temperatures of 1748 K (1475°C) and 1803 K (1530°C), respectively. These same

spheres floated in the A14Y melt at 2.5 GPa and 3.0 GPa at temperatures of 2023 K (1750°C) and 2048 K (1775°C), respectively. Increasing in sphere density, Fo_{90} spheres sank in this composition at 1.5 GPa and 1803 K (1530°C), were neutrally buoyant at 2.5 GPa and 1803 K (1530°C), and floated at 3 GPa and 2048 K (1775°C) placing tight constraints on the density bracket. A 1 GPa density bracket was also constrained with the sinking of Fo_{83} spheres at 3 GPa and 1973 K (1700°C) followed by the floating of these spheres at 4 GPa and 2023 K (1750°C). In order to further constrain this melt density beyond the pressures relevant to the lunar interior, we observed the sinking of garnet spheres ($Py_{66}Al_{12}Gr_5Sp_{16}$) at 6 GPa and 2248 K (1975°C) and a neutral buoyancy of these spheres at 7.5 GPa and 2423 K (2150°C). More experiments above 7.5 GPa are needed to place tighter constraints on the density of this melt.

Similarly to A15C, 2173 K (1900°C) is too high of a temperature to make an accurate estimate of density crossovers between the A14Y melt and its equilibrium pyroxene and olivine. There are currently no phase diagram data available on this composition where olivine and pyroxene are seen on the liquidus. Therefore, we estimated the MSP for A14Y by using the MSP's of A15C and A17O. Assuming the MSP of A14Y lies somewhere in between these two compositions, we chose the MSP to be at 2.3 GPa and 1823 K (1550°C). Figure 6 shows the density data for this melt at 1823 K (1550°C) with the corresponding density crossovers. Like A15C, a BM EOS is not an accurate depiction of the density of this melt. Therefore, we constructed two straight lines through our data set: one assuming the calculated 1-bar density and one assuming a lower 1-bar density.

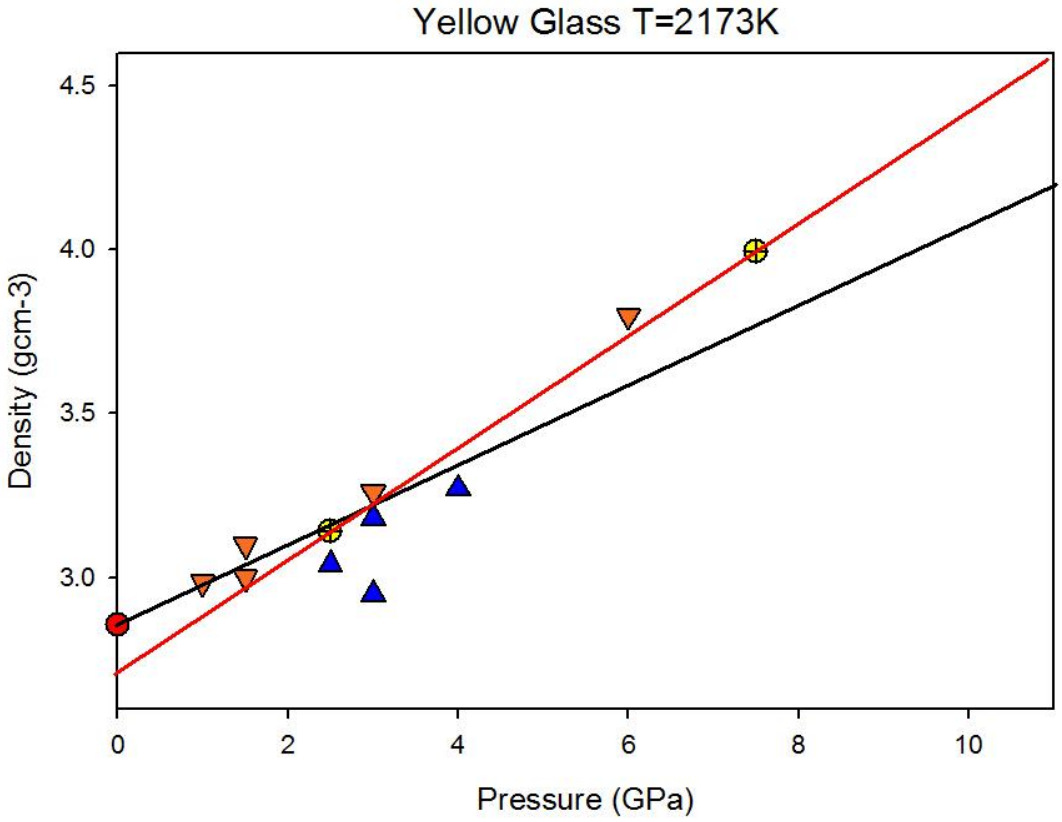

Figure 5. *Experimental results for yellow glass at T=2173 K (1900°C).* The calculated 1-bar density for this composition (red circle) at 1900°C is 2.85 g/cm^3 (Lange and Carmichael, 1987; Ochs and Lange, 1999). Downward pointing orange triangles represent sinks, upward pointing blue triangles represent floats, and circles represent neutral buoyancy points. The black line represents the best fit linear line to the current data anchored at the calculated 1-bar density. The red line shows a better linear fit to the data assuming a lower 1-bar density (~2.70 g/cm^3).

The density melt curve constructed by anchoring it at the calculated 1-bar density (black line in Figures 5 and 6) has a density crossover with its equilibrium pyroxenes at ~2.6 GPa. Using the equilibrium olivines calculated from the Toplis (2005) model, this melt has a crossover with its equilibrium olivines at ~3.2 GPa. However, using equilibrium olivines from the Ulmer (1989) model, the density crossover between melt and its equilibrium olivines occurs at ~3.6 GPa. If we examine the melt density curve assuming a lower 1-bar density than the calculated one (red line in Figures 5 and 6), as the actual 1-bar density of this melt is still unknown, these density crossovers occur at

different places: the density crossover between the melt and equilibrium pyroxenes is at ~3.2 GPa, and the density crossover between melt and equilibrium olivines is ~3.6 GPa (Toplis model) or ~3.9 GPa (Ulmer model). Although there are multiple density crossovers between this melt and its equilibrium mineral assemblages, regardless of the initial 1-bar density anchor, these crossovers occur at depths greater than that of the selected MSP; implications of which will be discussed later in this paper.

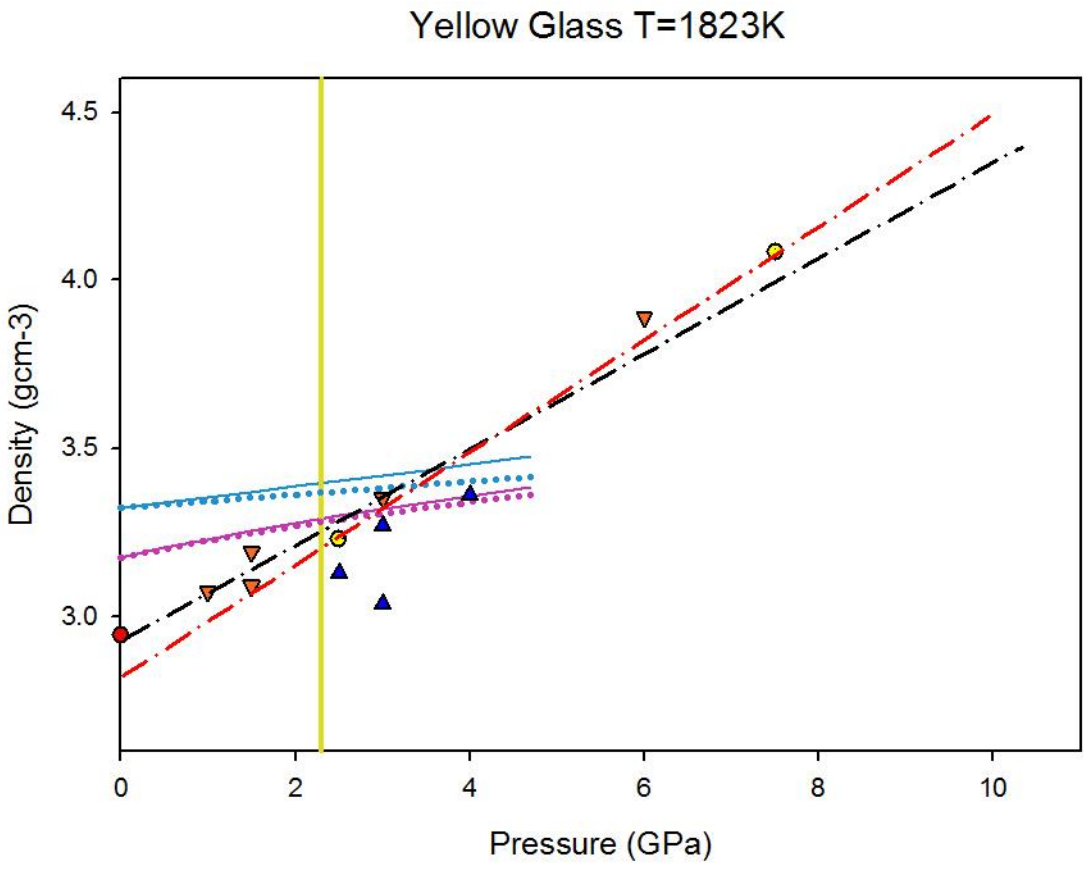

Figure 6. *Experimental results and density crossovers for yellow glass at T=1823 K (1550°C).* The calculated 1-bar density for this composition at 1550°C is 2.94 g/cm^3 (Lange and Carmichael, 1987; Ochs and Lange, 1999). Symbols are the same as Figure 5. The pink lines show the densities of equilibrium pyroxenes for this composition and the blue lines show the equilibrium olivines. The solid lines are from Ulmer (1989) and the dotted lines are from Toplis (2005). The yellow solid line shows the approximated MSP at 2.3 GPa.

Four of our experiments on yellow glass (A14Y) did not melt completely, resulting in near-liquidus garnets being present in the charges. Two of these experiments

were at 6 GPa, one at 7.5 GPa and one at 8.5 GPa with corresponding temperatures of 2148 K (1875°C), 2248 K (1975°C), 2348 K (2075°C), and 2373 K (2100°C), respectively. The compositions of these garnets are $Py_{61}Al_{19}Gr_{20}Sp_{0,}$ $Py_{66}Al_{21}Gr_{12}Sp_{1,}$ $Py_{67}Al_{20}Gr_{12}Sp_{1,}$ and $Py_{68}Al_{19}Gr_{12}Sp_{1,}$ respectively for the four experiments (Table B-5). A preliminary phase diagram for this composition is shown in Figure 7. We hesitate to draw a liquidus line on this diagram as our experimental results only indicate near liquidus garnets. However, based on melt composition and other phase diagrams for similar compositions, there should be a range of pressure where olivine is the stable liquidus phase and another where pyroxene is the stable liquidus phase. When a new mineral is introduced on the liquidus, this will change the slope of the liquidus line. Also, as these minerals crystallized during a 30 second run, we cannot be sure that they are the equilibrium minerals for this melt. We therefore present the data as is in Figure 7 for a graphical representation. Future work will involve characterizing a full phase diagram over the pressure range relevant to the Moon (up to 4.7 GPa) as a function of oxygen fugacity (fO_2).

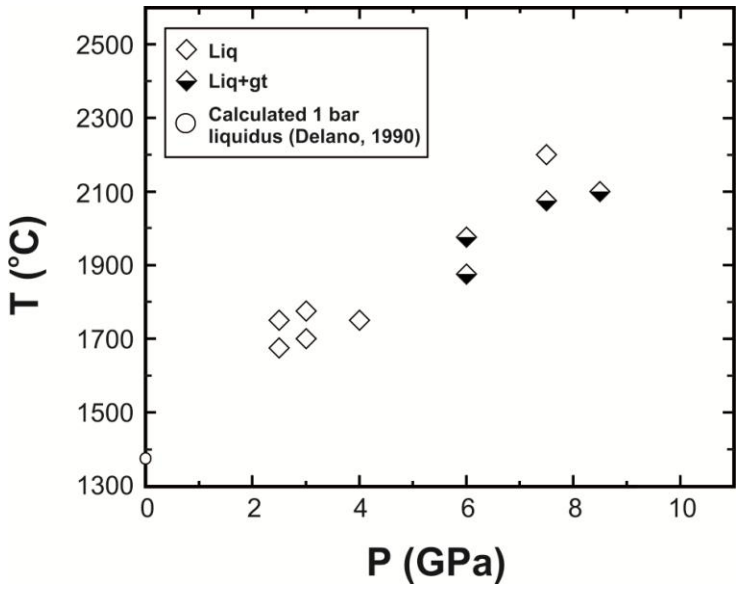

Figure 7. *Phase diagram for A14Y.* Using the experimental results from this study we have constructed a preliminary phase diagram for this composition. No lines have been added to the plot and further experimental data where we can assure equilibrium has been reached are needed.

3.3 Orange Glass

Experimental results for this composition (A17O) are summarized in Table B-3 and Figure 8. Experimental charges are shown in Figure B-6. The PC experiments conducted previously by van Kan Parker et al. (2011) were completed in the high pressure lab here at UNM with the talc cell setup. However, we have shown through SIMS analyses of "anhydrous" experiments in talc cells conducted in this same lab that there was on average 2.5-3 wt% water present in the experiments (Vander Kaaden et al., 2012). This additional water content is attributed to contamination from the talc cell. Previous studies have investigated the effect of water on melt density. One of these studies, Agee (2008), found that when 5 wt% H_2O was present in the experiments with a starting composition of 50% komatiite and 50% fayalite, the density difference between this melt and the anhydrous equivalent was 0.192 g/cm^3. Assuming the density difference is directly proportional to water content, we calculated the density difference between an

anhydrous melt and one with 3 wt% H_2O present. As all density experiments on the lunar glasses should be under anhydrous conditions, the PC data from van Kan Parker et al. (2011) was corrected by increasing the reported density values by 0.1152 g/cm^3 after Agee (2008).

We report four new data points for this composition at higher pressures. Pyrope-rich garnets ($Py_{60}Al_{37}Gr_3Sp_0$) were neutrally buoyant in the orange glass melt at 6.9 GPa and 2173 K (1900°C) and floated at 8 GPa and 2223 K (1950°C). Garnet spheres with the composition $Py_{34}Al_{57}Gr_5Sp_4$ sank in this melt at 8 GPa and 2373 K (2100°C). A sink at 10 GPa and 2423 K (2150°C) with $Py_{49}Al_{31}Gr_{19}Sp_1$ garnets was also observed. These data provide a new density bracket at 8 GPa and place further constraints on the density of this melt. We also report near liquidus mineral phases present in two experiments (Table B-5). At 6 GPa and 2273K garnets were present with a composition of ~$Py_{66}Al_{20}Gr_{14}Sp_0$, and at 8 GPa and 2373K garnets were present with a composition of ~$Py_{70}Al_{17}Gr_{13}Sp_0$.

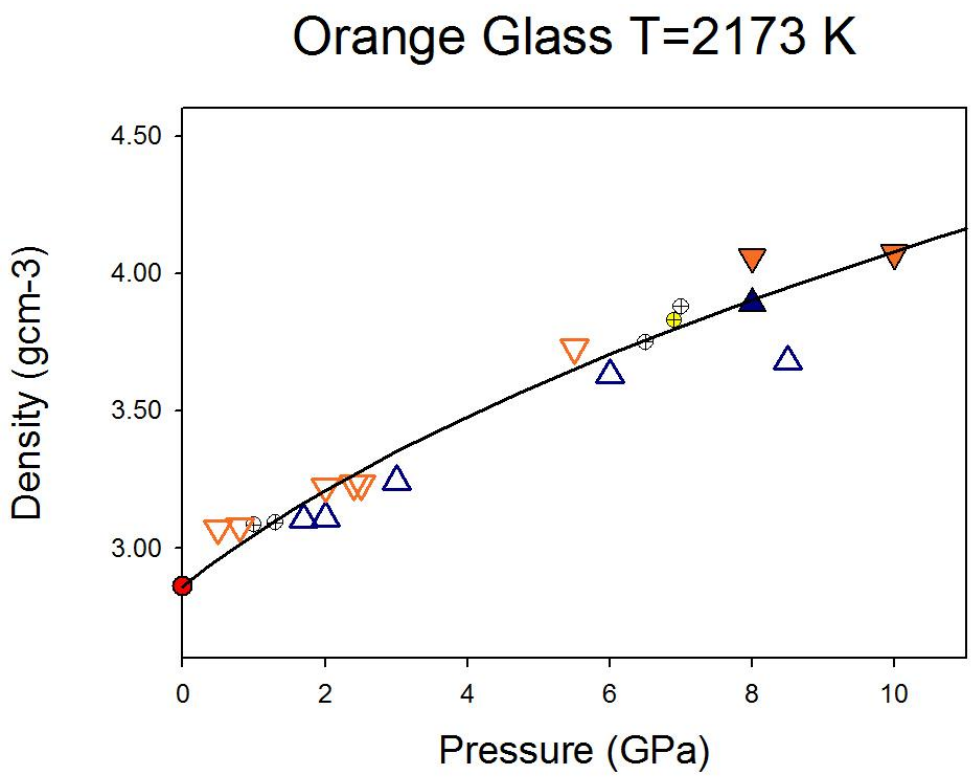

Figure 8. *Experimental results for orange glass at T=2173 K (1900°C).* The calculated 1-bar density for this composition (red circle) at 1900°C is 2.86 g/cm^3 (Lange and Carmichael, 1987; Ochs and Lange, 1999). Downward pointing orange triangles represent sinks, upward pointing blue triangles represent floats, and circles represent neutral buoyancy points. Filled data points are from this study and open data points are from van Kan Parker et al. (2011). The black line represents the 3rd order Birch-Murnaghan Equation of State best fit to the data when K′=4 and K_T=13.8 GPa. These data have not been corrected for H_2O contamination from the talc-pyrex cells during the PC experiments.

Krawczynski and Grove (2012) showed that A17O has two multiple saturation points (MSP) depending on fO_2. When fO_2 is IW + 1.3 (1.3 log units above the Iron-Wüstite buffer) the MSP of this composition with olivine and pyroxene on the liquidus is 2.5 GPa and ~1803 K (1530°C). However, when fO_2 is IW – 2.1 (2.1 log units below the Iron-Wüstite buffer) the liquid is saturated with both olivine and pyroxene at 3.1 GPa and ~1833 K (1560°C). Experimental data on the orange glass to date was corrected to 1803 K (1530°C) and 1833 K (1560°C) as shown in Figures 9 and 10, respectively to assess the possibility of density crossovers with equilibrium mineral assemblages. When

T=1803 K (1530°C) the Birch-Murnaghan EOS best-fit line, assuming K′=4, has a bulk modulus of 14.5 GPa (Figure 9). This line intersects the density curve for equilibrium pyroxenes at P≈1.6 GPa, a pressure lower than the MSP of this composition. The EOS line also intersects the olivine density curve in equilibrium with A17O at P≈2.17 GPa using the Toplis (2005) model and at P≈2.5 GPa using the Ulmer (1989) model. These density crossovers occur at pressures below and at the MSP for this composition, respectively. However, when T=1833 K (1560°C) the Birch-Murnaghan EOS best-fit line, assuming K′=4, has a bulk modulus equal to 14.6 GPa (Figure 10). Under these conditions, there is a density crossover between the A17O melt and its equilibrium pyroxenes at P≈1.7 GPa, again at a pressure lower than the MSP for this composition. There is a density crossover between the melt and its equilibrium olivines at P≈2.2 GPa (Toplis, 2005) and P≈2.6 GPa (Ulmer, 1989), both at pressures lower than the MSP pressure.

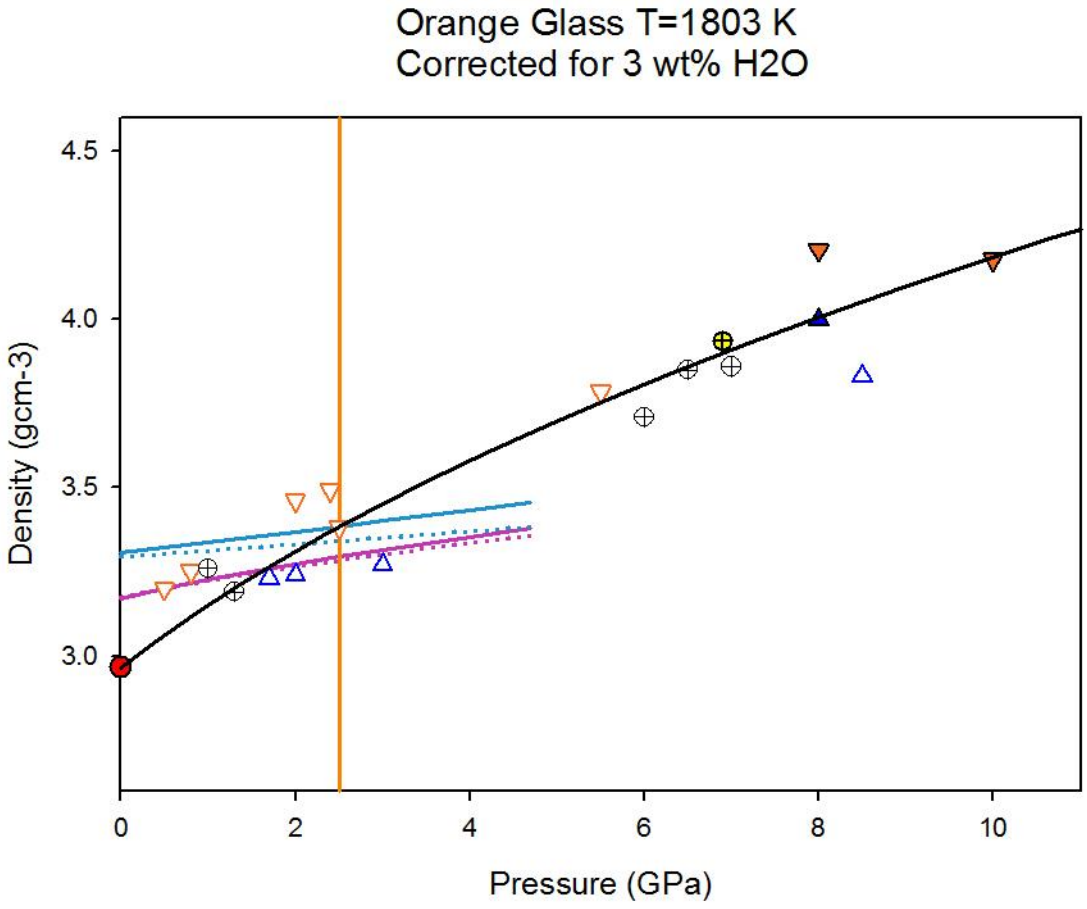

Figure 9. *Experimental results and density crossovers for orange glass at T=1803 K (1530°C).* The calculated 1-bar density for this composition (red circle) at 1530°C is 2.97 g/cm^3 (Lange and Carmichael, 1987; Ochs and Lange, 1999). Symbols are the same as Figure 8. The black line represents the 3rd order Birch-Murnaghan Equation of State best fit to the data when K′=4 and K_T=14.5 GPa. The pink lines show the equilibrium pyroxenes for this composition and the blue lines show the equilibrium olivines. The solid lines are from Ulmer (1989) and the dotted lines are from Toplis (2005). The orange solid line shows the approximated MSP at 2.5 GPa when the fO_2 is IW + 1.3. Data for experiments using talc-pyrex cells (van Kan Parker et al., 2011) have been corrected for 3 wt% H_2O.

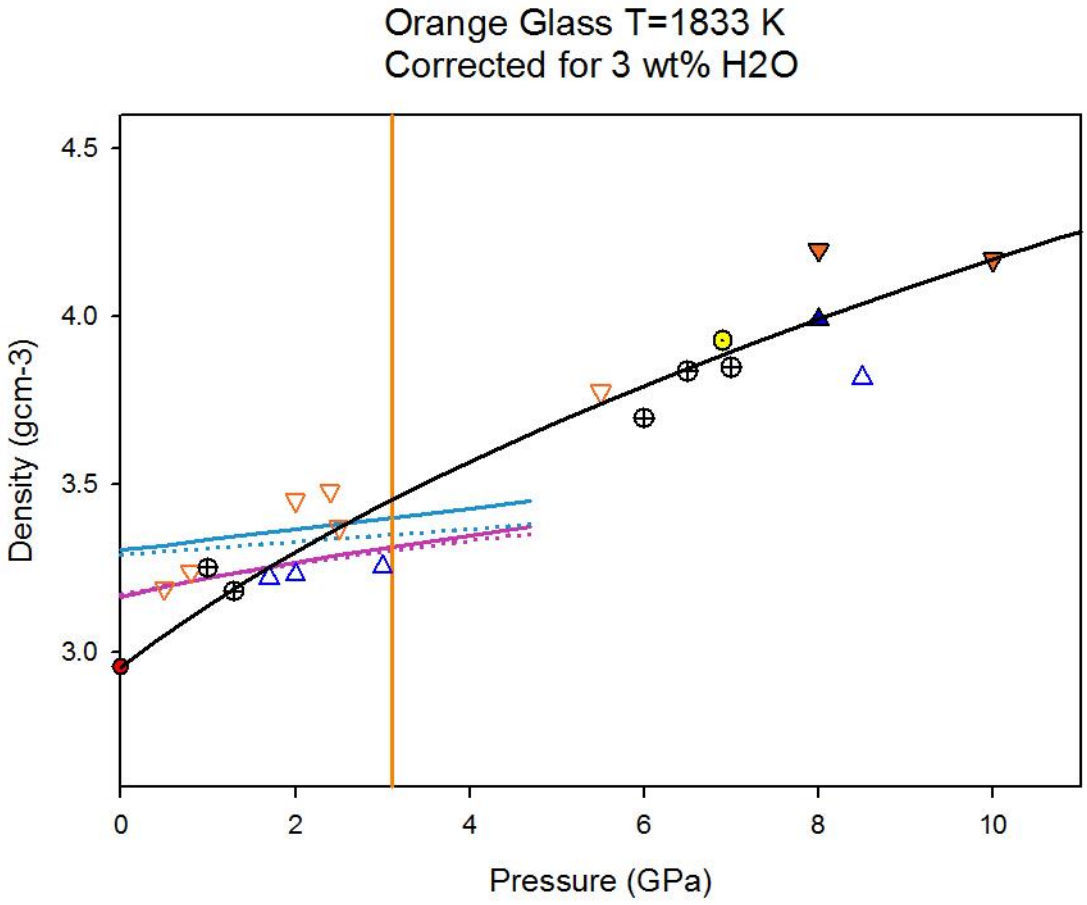

Figure 10. *Experimental results and density crossovers for orange glass at T=1833 K (1560°C).* The calculated 1-bar density for this composition (red circle) at 1560°C is 2.96 g/cm^3 (Lange and Carmichael, 1987; Ochs and Lange, 1999). Symbols are the same as Figure 8. The black line represents the 3rd order Birch-Murnaghan Equation of State best fit to the data when K′=4 and K_T=14.6 GPa. The pink lines show the equilibrium pyroxenes for this composition and the blue lines show the equilibrium olivines. The solid lines are from Ulmer (1989) and the dotted lines are from Toplis (2005). The orange solid line shows the approximated MSP at 3.1 GPa when the fO_2 is IW -2.1. Data for experiments using talc-pyrex cells (van Kan Parker et al., 2011) have been corrected for 3 wt% H_2O.

3.4 Black Glass

All experimental results for the A14 black glass were reported by Circone and Agee (1996). However, to make this data set consistent with the new results reported here, we have corrected the data to both 2173 K (1900°C) and 1703 K (1430°C), the standard temperature used in this study and the MSP temperature, respectively. Table B-4 shows the new densities corrected for both temperatures. Figure 11 shows this data set corrected to 2173 K (1900°C). A 3rd order Birch-Murnaghan EOS best fit line can be

constructed, with K′=4.85 and a bulk modulus of 19.3 GPa. The calculated 1-bar density for this composition at 1703 K (1430°C) is 2.92 gcm^{-3} (Lange and Carmichael, 1987; Ochs and Lange, 1999).

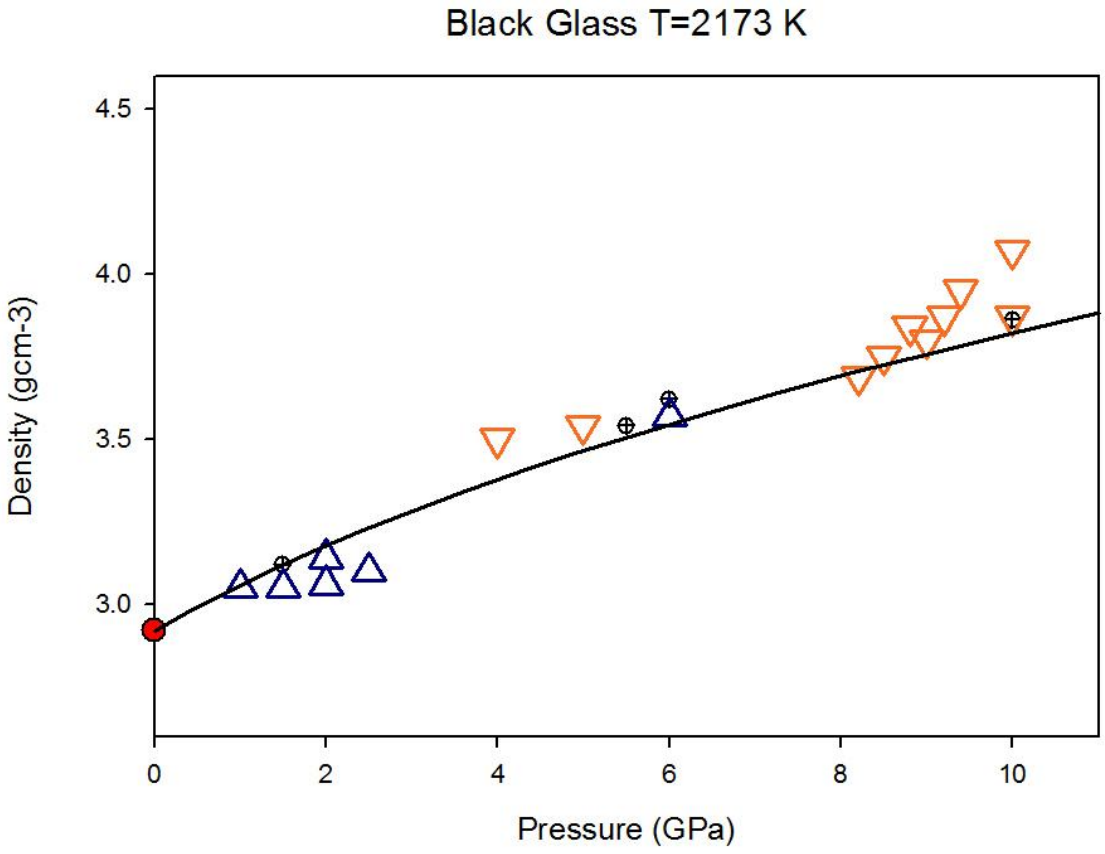

Figure 11. *Experimental results for black glass at T=2173 K (1900°C).* The calculated 1-bar density for this composition (red circle) at 1900°C is 2.92 g/cm^3 (Lange and Carmichael, 1987; Ochs and Lange, 1999). Downward point orange triangles represent sinks, upward pointing blue triangles represent floats, and circles represent neutral buoyancy points. All data are from Circone and Agee (1996). The black line represents the 3rd order Birch-Murnaghan Equation of State best fit to the data when K′=4.85 and K_T=19.3 GPa.

Figure 12 shows the data set corrected to the MSP temperature of 1703 K (1430°C) (Wagner and Grove, 1997). A 3rd order Birch-Murnaghan EOS best fit line can be constructed, assuming K′=4 and a bulk modulus of 23.4 GPa. The calculated 1-bar density for this composition at 1703 K (1430°C) is 3.085 gcm^{-3} (Lange and Carmichael, 1987; Ochs and Lange, 1999). For this composition, the equilibrium pyroxene densities

are very similar, regardless of which model is used; however, the equilibrium olivines vary depending on the model. Using the best fit line show in Figure 12, there is a density crossover between A14B and its equilibrium pyroxenes at ~1.3 GPa and ~1.7 GPa according to the calculations from the Toplis (2005) and Ulmer (1989) models, respectively. There is a much higher pressure difference between the equilibrium olivines calculated from the two models. The density of this melt has a crossover with its equilibrium olivines calculated from Toplis (2005) at ~2.3 GPa, whereas the crossover is at ~3.5 GPa using the Ulmer model. Out of these various crossovers, the only one that occurs at depths shallower than the MSP at 1.5 GPa is that of the equilibrium pyroxenes calculated from Toplis (2005).

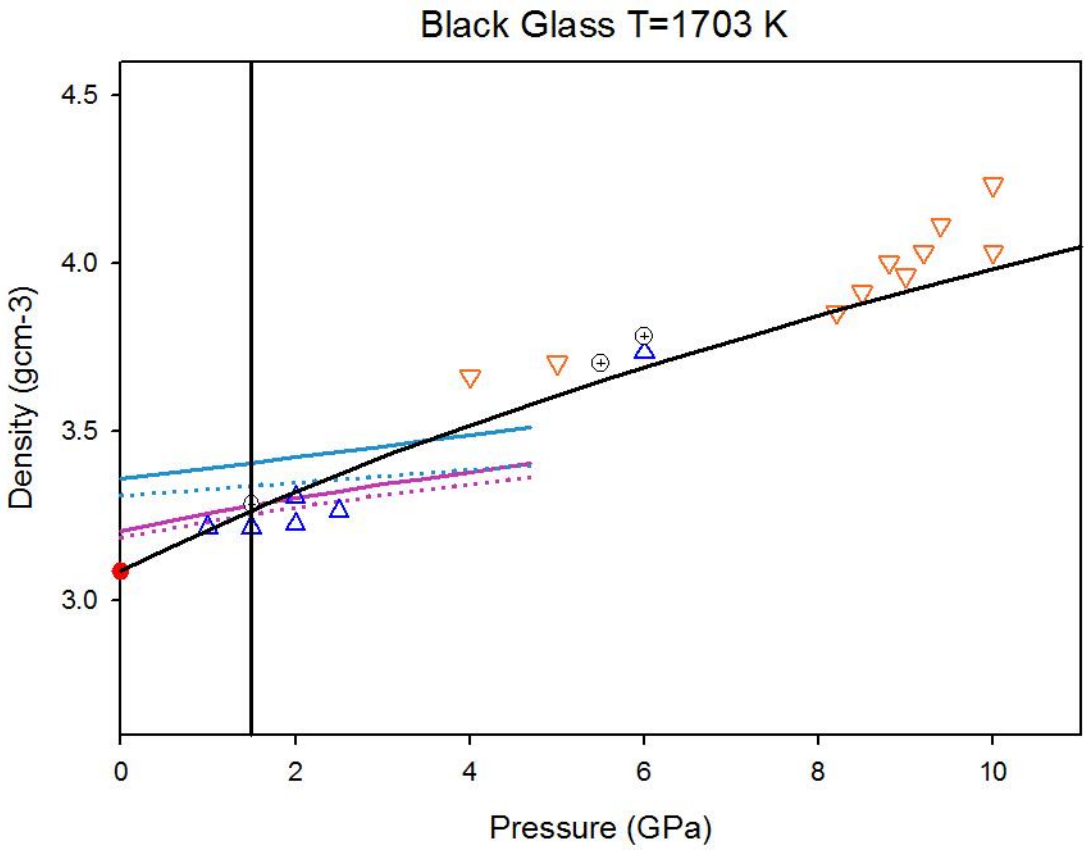

Figure 12. *Experimental results and density crossovers for black glass at T=1703 K (1430°C)***.** The calculated 1-bar density for this composition at 1430°C is 3.09 g/cm^3 (Lange and Carmichael, 1987; Ochs and Lange, 1999). Symbols are the same as Figure 11. The pink lines show the equilibrium pyroxenes for this composition and the blue lines show the equilibrium olivines. The solid lines are from Ulmer (1989) and the dotted lines are from Toplis (2005). The black concave line represents the 3rd order Birch-Murnaghan Equation of State best fit to the data when K′=4 and K_T=23.4 GPa. The black solid vertical line shows the approximated MSP at 1.5 GPa.

4. Discussion

4.1 Compressibility of Molten Lunar Volcanic Glasses

Our data show that the compressibility of the lunar volcanic glasses varies across the compositions investigated, which we attribute to the differences in TiO_2 content of these volcanic glasses. All of the compression curves we discuss in this and the following section (4.2) were calculated at the MSP temperature for the composition of interest (Table 4) therefore reflecting the effect of pressure on the change in liquid density. Table

3 shows the change in slope as a function of pressure for the glasses of interest. From this data, we report that the slope of A15C also remains fairly constant around 0.13-0.14 g/cm^3/GPa from 0-10 GPa. This is not consistent with previously reported data from Smith and Agee (1997) who determined a slope of 0.093 g/cm^3/GPa from 0-3 GPa. However, with the new data reported here at higher pressures, we are confident in the compression curve that we have established and believe we have placed better constraints on the density and compressibility of this glass. Similarly to the green glass, the A14Y data presented here is the first reported data for the yellow glass so comparisons to previous studies cannot be made. However, Table 3 shows the slope of A14Y remains fairly constant around 0.15-0.16 g/cm^3/GPa over the pressure range of interest (0-10 GPa).

In contrast to the glasses with low TiO_2 contents, A17O exhibits similar behavior to A14B in having a steep slope initially which then decreases with pressure. The shape of the curve is in agreement with previously published data, however the steepness of the slope is greater than that previously reported. Van Kan Parker et al. (2011) report an initial density increase of ~0.07-0.08 g/cm^3/GPa. However, our data shows an initial density increase of 0.18 g/cm^3/GPa decreasing to about 0.09 g/cm^3/GPa around 10 GPa. We attribute this vast difference in compressibility to two factors. First, the low-pressure (PC) data presented in this study for the orange glass has been corrected for 3 wt% H_2O (discussed in section 3.3). Secondly, we have contributed four more data points to A17O at higher pressure (above 6 GPa), which has a large impact on the shape of the compression curve. Reexamination of Table 3 shows the initial slope of the A14B is 0.12 g/cm^3/GPa. This is in close agreement with the slope observed by Circone and Agee

(1996) of 0.13 g/cm^3/GPa. As pressure increases, the slope becomes shallower producing a concave downward curve, also in agreement with previously published data (Circone and Agee, 1996).

Table 3. *Compressibility of lunar glasses.* The slope of each compression curve is given below over multiple pressure increments in g/cm^3/GPa. All slopes were determined at the MSP temperature for the respective composition. *Average A17O refers to the average slope of both OG compression curves at varying oxygen fugacities. **Average A14O refers to the average slope of the two compression curves in Figure 6 with varying 1 bar densities.

	0-2 GPa	2-4 GPa	4-6 GPa	6-8 GPa	8-10 GPa
A14B	0.12	0.10	0.09	0.08	0.07
Average A17O*	0.18	0.14	0.11	0.10	0.09
Average A14Y**	0.16	0.16	0.15	0.15	0.16
A15C	0.14	0.14	0.14	0.14	0.13

To look at the relative compressibility of these glasses, Figure 13 has been constructed which shows two plots of density/initial density (ρ/ρ_0) versus pressure (P). By plotting ρ/ρ_0 on the y-axis instead of ρ, we can anchor all of the compositions at the same starting point (1 on the y-axis). Figure 13A shows the compressibility differences between A14B, A17O, and A15C glasses. The yellow glass has been omitted from this graph to only display the data sets that have been constrained up to at least 10 GPa. This data shows that with increasing TiO_2 content, we see increasing flattening of the compression curve. However, the composition with the least TiO_2 (A15C) remains relatively constant in terms of slope. Implications of the effect of TiO_2 content on melt compressibility are discussed in the next section. Figure 13B shows the same 3 curves from Figure 13A but has A14Y plotted on it as well. The solid line up to 6 GPa shows the extend of constraints that we have placed on this composition assuming the calculated 1-bar density (Lange and Carmichael, 1987; Ochs and Lange, 1999). Above 6 GPa, we have plotted possible positions for the continuation of this compression curve. It is

possible that the data remains on a straight line with a constant slope similar to A15C, or it may become concave downwards like A17O and A14B. Our hypothesis is that it will lie somewhere in between these two extremes, not remaining perfectly linear, but not becoming extremely concave. Further experimental data is needed to place better constraints on this composition at higher pressure. However, with this data we can conclude that the lunar glasses are more compressible than both komatiitic and peridotitic liquids with slopes of ~0.075 g/cm^3/GPa and 0.065 g/cm^3/GPa, respectively (Agee and Walker, 1988 & 1993).

Table 4. *Multiple saturation points.* This Table gives the pressure and temperature of the multiple saturation points for each lunar glass composition.

Lunar Volcanic Glass	P	T(°C/K)	Depth (km)[1]	Reference
Green Glass (A15C)	1.3	1520/1793	245	Wagner and Grove (1997)
Yellow Glass (A14Y)	2.3	1550/1823	510	Estimate This Study
Orange Glass (A17O)[2]	2.5	1530/1803	550	Krawczynski and Grove (2012)
Orange Glass (A17O)[3]	3.1	1560/1833	720	Krawczynski and Grove (2012)
Black Glass (A14B)	1.5	1430/1703	300	Wagner and Grove (1997)
[1]Estimated from Kennedy and Higgins (1975), [2]fO_2 is $\Delta IW + 1.3$, [3]fO_2 is $\Delta IW - 2.1$				

As we've shown, this new data places better constraints on the compressibility of the lunar glasses as a function of temperature and pressure. At low pressures (0-2 GPa) A17O is the most compressible compositions followed by A14Y, A15C, and A14B in order of decreasing compressibility, respectively. However, once we get above 2 GPa until 6 GPa, A14Y is the most compressible melt followed by A15C, A17O, and A14B. Assuming the yellow glass continues on a linear line similar to the green glass, currently this order of decreasing compressibility from A14Y to A14B should remain the same. Nevertheless, if the compression curve for A14Y becomes concave downward like the

other glasses with higher TiO_2 contents, we would expect the compressibility of the green glass to exceed that of the yellow glass giving us a compressibility order of A15C, A14Y, A17O, and A14B from most compressible to least compressible. It is interesting to note that this compressibility trend is consistent with increasing compressibility as TiO_2 content decreases, most likely due to the coordination state of Ti^{4+} in the melt.

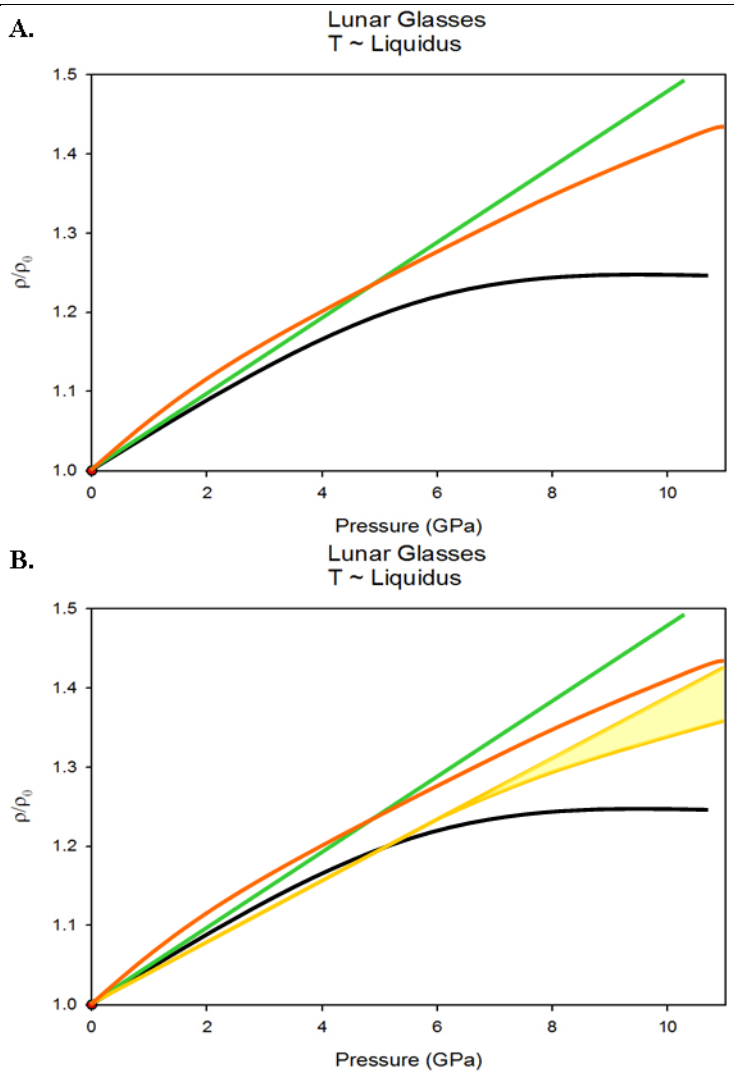

Figure 13. *Compressibility of lunar glasses.* The plots above show the trend in the slopes of the lunar glasses and therefore, their compressibility. The color of the line corresponds to the color of the glass. The shaded area for the yellow glass shows possible extensions of our current data points. Refer to text for full discussion.

4.2 Titanium Coordination and its Effect on Lunar Melt Density and Compressibility

We know the largest compositional difference between these three volcanic glasses is their TiO_2 content, Mg#, and SiO_2 content; however Ti^{4+} has the ability to exist in the silicate melt both as a network former and a network modifier (whereas Fe^{2+} is typically a network modifier and Si^{4+} is typically a network former under the experimental conditions we investigated). Over the compositional range of naturally occurring lunar glasses we have examined, an increase in TiO_2 content is generally accompanied by an increase in FeO content and a decrease in MgO and SiO_2. However, during this process, FeO is mostly replacing MgO and each component will remain octahedrally coordinated so this should not have an impact on melt compressibility. Also, SiO_2 should remain tetrahedrally coordinated up to at least 20 GPa (Williams and Jeanloz, 1988; Fukui et al., 2008). Therefore, we focus on the change in coordination of Ti^{4+} which has been shown to occur in 4-, 5-, and 6-fold coordination over the pressure range of interest (0-10 GPa) (Sandstrom et al., 1980; Greegor et al., 1983; Farges and Brown, 1997; Liu and Lange, 2001).

Titanium is a lithophile element with a molar mass of 47.90 g/mol and melting point of 1953 K. The coordination of Ti^{4+} is complex and poorly understood. According to Liu and Lange (2001), Ti^{4+} can occur in four-, five-, and six-fold coordination in crystalline compounds where four-fold is considered tetrahedrally coordinated, five-fold is an asymmetric square pyramid with one short Ti=O and four longer Ti-O bonds (Farges and Brown, 1997), and six-fold is considered octahedrally coordinated. Since the densities of silicate melts are largely governed by the geometrical packing and coordination of their network forming ions, the capacity of Ti^{4+} to shift coordination will

have a large impact on the melt densities (Liu and Lange, 2001). However, there is much disagreement among scientists as to the behavior of Ti^{4+} in melts.

X-Ray Absorption Spectroscopy data on TiO_2-SiO_2 glass by Sandstrom et al. (1980) indicate both tetrahedral and octahedral Ti^{4+} may occur in the glass. Their study indicates that Ti^{4+} is predominately 4-fold ($^{[IV]}Ti^{4+}$)when the melt has between 3.4-9.5 wt% TiO_2, relevant to the TiO_2 contents of the yellow glass and orange glass in this study. However, as the amount of TiO_2 increases, the ratio of 6-fold to 4-fold increases, indicating more $^{[VI]}Ti^{4+}$ is present. Using the same technique on TiO_2-SiO_2 glass, Greegor et al. (1983) are in close agreement with Sandstrom et al. (1980). Their results indicate when there is less than 0.05 wt% TiO_2, Ti^{4+} will be octahedrally coordinated. However, greater than 0.05 wt% TiO_2 up to 9 wt% TiO_2, Ti^{4+} will be tetrahedrally coordinated. This study agrees that with increasing TiO_2 (more than 9 wt%), the ratio of 6-fold to 4-fold increases, indicating more $^{[VI]}Ti^{4+}$ is present. Thus it is possible that silicate melts with high TiO_2 contents will show unusual compressibility changes as coordination in the melt shifts to higher values with increasing pressure. Contradictory to these studies however; Raman spectroscopy data by Mysen and Neuville (1995) indicate $^{[IV]}Ti^{4+}$ dominates in glasses along the $Na_2Ti_2O_5$-$Na_2Si_2O_5$ binary with about 20 wt% TiO_2.

Studies using x-ray absorption near edge structure (XANES) spectroscopy by Farges and Brown (1997) on natural volcanic glasses and tektites indicate Ti^{4+} is dominant in five-fold coordination ($^{[V]}Ti^{4+}$). According to this study, the more polymerized a glass is, the more $^{[IV]}Ti^{4+}$ (about 30-50%) is seen, whereas the less polymerized glasses show about 30-50% of the titanium as $^{[VI]}Ti^{4+}$ with the latter being the expected result for the ultramafic Apollo volcanic glasses. An exception to this trend

was seen in the Ti-poor glasses (<3 wt% TiO_2) studied by Farges and Brown (1997), equivalent to A15C, where $^{[IV]}Ti^{4+}$ was found to be dominate.

With numerous conflicting views on the coordination of Ti^{4+}, the most reasonable answer is Ti^{4+} most likely occurs in more than one coordination state in silicate melts (Mysen, 1987). A study by Greegor and Lytle (1983) of the Ti-site geometry in the lunar glasses by X-Ray Absorption Spectroscopy is in agreement with this observation. They also suggest the color changes in the lunar glasses could be the result of the changing coordination state of Ti^{4+}. As mentioned previously, TiO_2 is one of the largest compositional variation between the green, yellow, orange, and black glasses. Therefore, it has the potential to be the driving force behind the difference in compressibility and density observed in this and previous studies (Circone and Agee, 1996; Smith and Agee, 1997; van Kan Parker et al., 2011).

Figure 14 shows the experimentally determined density and compressibility curves for the lunar glasses. All glasses are plotted at the MSP for their respective composition (Table 4, above). Figure 14A shows the compression curves for A14B, A17O as a function of fo_2, A14Y as a function of the chosen 1-bar density, and A15C, in their respective colors. These lines correspond to the compression curves in the results section (3) above. From the A17O lines on Figure 14A, we can see that fo_2 has little effect on the melt density and compressibility for this composition. Figure 14B shows the same lines for A14B, A17O, and A15C as Figure 14A, however the density curve for A14Y is now represent slightly different. The solid line up to 6 GPa shows our current constrained data set. Similarly to the ρ/ρ_0 curves in Figure 13B, above 6 GPa we have constructed a series of curves that lie within the yellow shaded region for possible

extension of the yellow glass data set. Finally, Figure 14C, shows the data up to 10 GPa for the A14B, A17O, and A15C that we are confident with.

We can attribute the change in density and compressibility for these lunar glasses to their vastly different TiO_2 contents. Using the arguments discussed above, A14B (16.4 wt% TiO2) initially has more 6-fold coordinated Ti^{4+} present. Therefore it is more compressible at lower pressures where the remaining $^{[IV]}Ti^{4+}$ is most likely becoming $^{[VI]}Ti^{4+}$. However, once all of the $^{[IV]}Ti^{4+}$ is in 6-fold coordination, the compressibility decreases with increasing pressure as seen in Figures 13 and 14 and Table 3. A similar argument can be used to explain the compressibility of A17O. However, examination of the bulk moduli for these two compositions (A14B K_T=23.4 GPa and A17O K_T≈14.5 GPa when K′=4) shows that A17O is more compressible than A14B. This can be attributed to the lower amount of $^{[VI]}Ti^{4+}$ initially present in the orange glass. Therefore, as we increase pressure, there is a higher amount of $^{[IV]}Ti^{4+}$ going into $^{[VI]}Ti^{4+}$ than in A14B, increasing the compressibility of this melt. Figure 14 shows that the orange glass has a density crossover with the black glass at ~2.25 GPa, well within lunar pressures.

For A15C, Figures 2, 3, and 14 show the steep slope of this melt is maintained from 0-10 GPa. This observation is consistent with the fact that most, if not all, of the Ti^{4+} in this melt is in 4-fold coordination (Farges and Brown, 1997). Also, as shown in table 1, A15C has about 47 wt% SiO_2 in its' composition. Therefore, there are more Si atoms in A15C compared to the other glasses. Consequently, the melt structure of this composition has a lot more tetrahedral complexes in it compared to the other glasses which may have an additional impact on its' compressibility. For the yellow glass, we can make the same argument for the lower pressure (below 6 GPa) data. However, until

the data set is better constrained, at this point we cannot make any presumptions of the amount of $^{[IV]}Ti^{4+}$ versus $^{[VI]}Ti^{4+}$ in the melt. Figure 14C also shows the complete reversal in density of the lunar glasses at higher pressure. At lower pressure the melt with the highest TiO_2 content is the densest, as one would expect. However, at ~2.25 GPa, the density of A17O exceeds that of A14B. Following this at ~7.25 GPa the density of A15C exceeds that of A14B and at ~10.25 GPa, the density of A15C exceeds that of A17O. Although we have not measured the coordination of Ti^{4+} in our experimental charges, we can attribute this remarkable change in density at high pressures to the change in coordination state of Ti^{4+} in the melt structure.

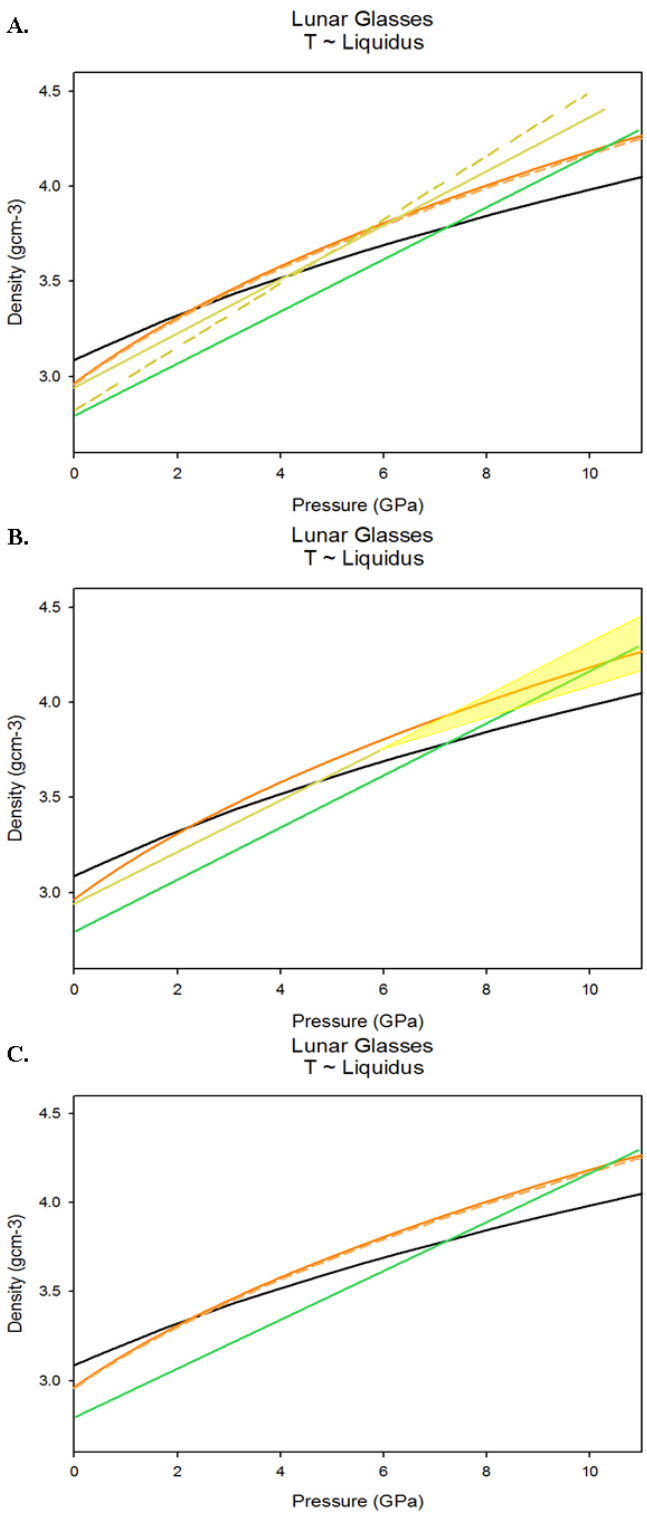

Figure 14. *Effect of TiO_2 on melt density.* Compressibility curves for the lunar glasses. The color of the line corresponds to the color of the glass **A.** The dotted orange line corresponds to an fO_2 of IW -2.1 and the solid orange line corresponds to an fO_2 of IW +1.3. The yellow dotted line is the best fit assuming a lower 1-bar density than the calculated one (solid yellow line). **B.** The shaded area for the yellow glass shows possible extensions of our current data points. **C.** Compression curves up to 11 GPa for the three lunar glasses with complete data sets to date. Refer to text for full discussion of this Figure.

4.3 Eruptability of Molten Lunar Volcanic Glasses

The density crossovers of main concern when discussing the eruptability of a melt occur when a melt becomes denser than its equilibrium crystals, hindering it from rising towards the surface. These density inversions are an important aspect of lunar volcanism that need to be considered when determining the eruptability of a magma. All of the lunar glasses discussed in this study were found on the surface of the Moon during the Apollo missions; therefore, conditions existed that allowed all of them to erupt. However, fundamental questions in regards to these conditions remain unanswered. Did the glasses erupt strictly as a result of buoyancy forces? If the glasses were not able to erupt by buoyancy alone, what other factors were involved in bringing them to the surface? The experiments conducted on these glass compositions allow us to directly determine the pressure-temperature (P-T) conditions of density crossovers in the lunar interior and this information allows us to make important advances in answering some of the outstanding questions mentioned above.

At high pressures, it has been predicted that lunar and terrestrial magmas can become denser than their coexisting crystals (Stolper et al., 1981; Delano, 1990; Agee, 1998). If a magma is denser than its equilibrium crystals, then it should become negatively buoyant and unable to erupt, sinking deeper into the interior of the Earth of Moon (Delano, 1990; Wagner and Grove, 1997). By constraining the depths at which these inversions occur, we can place tighter constraints on the depths of origin of the lunar glasses in this study. The equilibrium crystals of importance for these glasses are olivine and pyroxene as they make up the majority of the lunar mantle.

We calculated the compositions of olivine and pyroxene that would be in equilibrium with the lunar glasses of interest through use of the models of Ulmer (1989), Toplis (2005), and the program QUILF (Andersen et al., 1993). For a complete discussion on this process the reader is referred to Section 2.5 and Appendix A. As discussed in the Results section, each lunar glass has multiple density crossovers with its equilibrium minerals. However, the question becomes, which crossovers hinder the eruption of these melts? To answer this question, we take into account the multiple saturation point (MSP) of each composition (Table 4). A MSP occurs when the coexistence of two minerals, in this case olivine and pyroxene, are present at the same pressure along the liquidus. This pressure is taken to represent the average depth at which the melt separates from its equilibrium minerals and rises to the surface, or its depth of origin (Asimow and Longhi, 2004). As we can see from Figures 3 and 6, density crossovers between the equilibrium minerals and the melts of A15C and A14Y, respectively, both occur at pressures greater than the experimentally-determined MSP's for each respective composition. Therefore, these glasses should be able to rise through buoyancy forces alone. On the other hand, by reviewing Figures 9, 10, and 12, we can see that the density crossovers between A17O and A14B, respectively, and their equilibrium minerals occur at depths shallower than their MSP's. For A17O, the melt has density crossovers with both its equilibrium olivines and pyroxenes at depths shallower, or at the equivalent depth of, the MSP for this composition. Therefore, this glass will not erupt solely on the basis of buoyancy factors alone and other possibilities need to be examined, as we discuss below (section 4.3.1).

For A14B, on the other hand, density crossovers only occur with the equilibrium pyroxenes at depths shallower than the MSP for this melt. Therefore, we can calculate, based on the density of the equilibrium pyroxene (3.25 g/cm^3), equilibrium olivine (3.34 g/cm^3), and the density of the melt (3.26 g/cm^3 at the MSP of 1.5 GPa), the mineral proportions required for the A14B density crossover. By doing so, we find the Apollo 14 black glass (A14B) could erupt by buoyancy forces alone, if the surrounding mantle had ≤ 87% pyroxene and ≥ 13% olivine. By examining the predicted mineralogy of the cumulate pile after crystallization of the LMO, the mineral proportions suggested here are not unreasonable and favor the eruption of A14B (Snyder et al., 1992; Shearer et al., 2006; Elardo et al., 2011; Elkins-Tanton et al., 2011; Rapp and Draper, 2012).

4.3.1 Eruption of A17O

Krawcynski and Grove (2011) experimentally determined MSP's for the A17O glass as a function of oxygen fugacity. The Apollo 17 orange glass has density crossovers with its equilibrium pyroxenes and olivines either at, or at depths shallower than, the MSP (2.5-3.1 GPa) for this composition. Therefore, this melt should be negatively buoyant with respect to its surrounding mantle and sink deeper into the lunar interior. However, as we have samples of this composition collected at the surface, we know that A17O was able to erupt. Consequently, other factors must have allowed for the eruption of this composition. In the past, it has been suggested that volatiles can play a large role in the eruption of the lunar glasses (Sato, 1979; Fogel and Rutherford, 1995; Elkins-Tanton, 2003b). This idea has been ruled out for the eruption of A17O as there are just not enough volatiles in the source regions to bring this melt from such great depths

(Hauri et al., 2011; Saal et al., 2008). Volatiles can aid in the final stages of eruptions as discussed in Section 4.3.2.

Although the A17O melt should be negatively buoyant, Hess (1991) presented a model that could allow negatively buoyant melts to reach the surface, one we will defer to here for the origin of A17O. The reader is referred to Hess (1991) for full model details and calculations. In this model the negatively buoyant melt can be trapped within an ascending lunar diapir as long as the ascent velocity of the diapir is greater than the velocity of the downward moving melt. As the diapir rises adiabatically to the surface, the melt can either be brought to depths shallower than its neutral buoyancy zone where it segregates from the diapir and rises based on buoyancy forces, or the melt will be trapped above the lower thermal boundary layer of the diapir (Hess, 2000). If the latter occurs, the melt can descend into the lunar interior relative to both the diapir and the surrounding mantle. Once this melt gets to higher pressures, it will crystallize and stall its descent. However, these crystallization products are then carried back upwards and remelted. This process of rising, sinking, crystallizing, and rising again can continue until the rising diapir reaches a point above the neutrally buoyant zone for the melt and the melt can segregate out of the diapir and rise to the surface. Through use of this model, we assume the glasses produced in this manner are collections of near primary magmas which are the products of polybaric melting (Longhi, 1990) (i.e. melts produced over a range of depths).

4.3.2 Effect of Volatiles on Eruption of Lunar Glasses

Volatiles have always been an important topic of concern in the discussion of the eruptability of the lunar glasses, which are believed to be the product of lunar fire

fountaining eruptions (Sato, 1979; Fogel and Rutherford, 1995; Elkins-Tanton et al, 2003b). The most important equilibrium gas phases that will be present at the fo_2 ranges of the moon (IW to IW-1) are H_2 and H_2S (Sharp et al., 2012; Zhang, 2011; Greenwood et al, 2012; Elkins-Tanton and Grove, 2011). Minor amounts of HF, HCl, and H_2O with perhaps some C species can also be considered (Fegley and Swindle, 1993; Rutherford and Papale, 2009; Fogel and Rutherford, 1995; Elkins-Tanton et al., 2003b). For the lunar glasses, water which would have been dissolved in the melts as OH and degassed as H_2, is probably the most prominent volatile in aiding the eruption of these glasses (Sharp et al., 2012).

Until recently, the Moon's interior was believed to be anhydrous. Table 5 summarizes recent studies which suggest the presence of indigenous H_2O contents in the Moon. Saal et al. (2008) analyzed the volatile content in lunar glass beads ranging from very-low to high TiO_2 content. The study found there is a decrease in H_2O concentration from about 30 ppm to 14 ppm from the core of the beads to the rim suggesting that H_2O is indigenous to the glasses and not the result of solar wind implantation. Other estimates of H2O content of the lunar interior are based on OH analyses on apatite grains. If H_2O is present in the Moon it could have increased the amount of flux melting at depths significant to the production of lunar glasses and the degassing of this volatile may have acted as another driving force aiding in the eruption of these primitive glass beads. However the highest amount of water measured in lunar glass beads to date was on the orange glass which has 1410 ppm, (Hauri et al., 2011) and this is still too little water to decrease the density of the A17O melt composition so that it can leave its source region and rise through the lunar interior (Agee, 2008). Hauri et al. (2011) also reported 80-78

ppm fluorine, 612-877 ppm sulfur and 1.5-3.0 ppm chlorine within melt inclusions of olivine grains in the lunar glasses. The additive effects of these volatiles will aid in the fire-fountaining (or "spraying" effect) during the eruption of the lunar glasses and degassing of these volatiles, but it is important to note that these volatiles, on their own, will not be able to get a negatively buoyant melt such as the orange glass to the surface of the Moon.

Table 5. *Water content of the Moon.* (Adapted from Elkins-Tanton and Grove, 2011)

Samples Studied	Observation	Inferred magma water content	Inferred melting source region water content
Mare Basalts	3000 to 6000 ppm water in apatite crystals in 12039[a]		2 to 12 ppm water[a]
Basalts with KREEP component	220 to 1000 ppm OH in apatite crystals in alkali suite clast 15404,51[b] 4000 to 7000 ppm OH in low-titanium NWA 2977[b] ~1550 to 2405 ppm water in apatites in 14053[d]	2 to 28 ppm water[b] 70 to 170 ppm water[b,c]	60 to ~830 ppb water[b] 2 to 5 ppm water[b] 100 to 200 ppm water[d]
Highlands crust with KREEP component	~100 ppm water in apatite crystals in 14305[a]		
Ultramafic glasses	4 to 46 ppm water in glass beads[e] 615 to 1410 ppm water in glass beads[g]	260 to 745 ppm water[e]	2 to 200 ppm water[b,f] 79 to 409 ppm water[g]

[a] Greenwood et al. (2011), [b] McCubbin et al. (2010a), [c] McCubbin et al. (2010b), [d] Boyce et al. (2010), [e] Saal et al. (2008), [f] Elkins-Tanton and Grove (2011), [g] Hauri et al. (2011)

5. Conclusion

As a result of our study, the density and compressibility of A15C and A17O have been determined up to at least 10 GPa, and A14Y up to 6 GPa. More experiments are needed to extend the range of A14Y up to 10 GPa. By extending this data set to 10 GPa we can not only place better constraints on the bulk modulus (K_T) of this melt, we can see if TiO_2 impacts the melt density and compressibility at higher pressures. Comparison of these glasses with each other and A14B which has been previously characterized by

Circone and Agee (1996) shows that with increasing pressure, melts with lower TiO_2 contents become more compressible. This causes a complete reversal in relative densities from lower pressures to higher pressures resulting in the most TiO_2-rich composition becoming the least dense at higher pressures. We attribute this change in density from 0-10 GPa to the coordination state of Ti^{4+} from $^{[IV]}Ti^{4+}$ to $^{[VI]}Ti^{4+}$ in the melts with higher TiO_2 (A17O and A14B). With these new data we have determined density crossovers for these lunar glasses between the given melt composition and its equilibrium olivines and pyroxenes calculated from Toplis (2005), Ulmer (1989) and the program QUILF (Anderson et al., 1993). Based on these density crossovers, with the exception of A17O, the lunar glasses discussed should be able to erupt based on neutral buoyancy forces alone. However, for A17O, as some density crossovers occur at depths shallower than A17O's MSP, so we must call on the rising diapir model of Hess (1991) for eruption of this melt. Although volatiles may provide a driving force for spraying of the lunar fire-fountaining eruptions, there are not enough volatiles in the source regions of these glasses to decrease the density sufficiently for them to be able to migrate towards the surface through the lunar mantle. Future work for this project will include placing better constraints on A14Y at higher pressures (above 6 GPa), experimentally determining the density and compressibility of the Apollo 15 red glass (A15R) which has 13.8 wt% TiO_2 (Delano, 1986) to try and further our understanding of the coordination state of Ti^{4+} in the melt, and constructing a phase diagram for A14Y to determine the correct MSP of olivine and pyroxene and see if there is any variation in phases present as a function of fO_2.

Appendices

Appendix A-Methods

This appendix contains schematics for both the PC and MA experimental designs. Step-by-step details for the calculations of equilibrium pyroxenes and olivines present in the lunar mantle with each melt composition are discussed.

Experimental Design

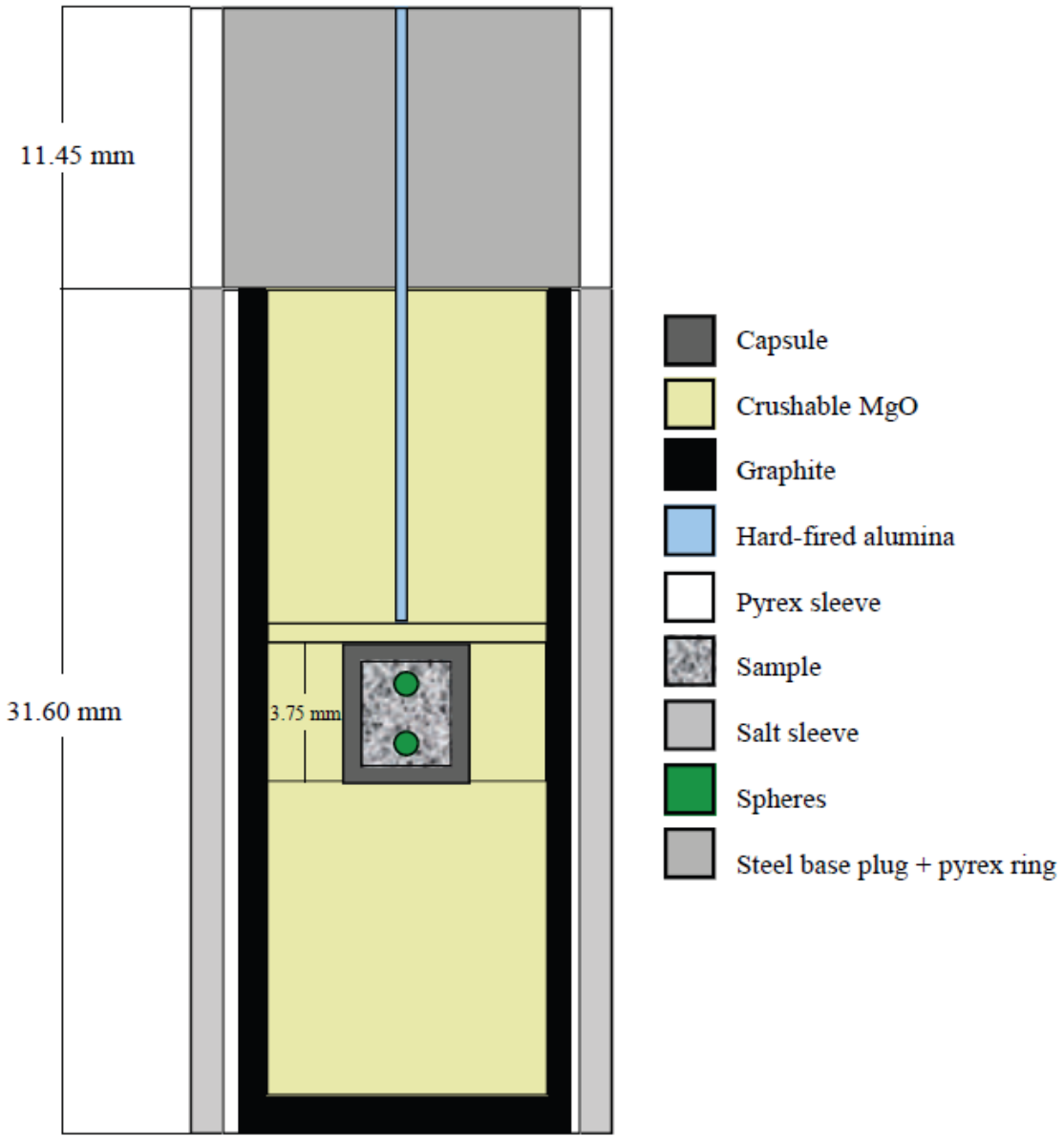

Figure A-1. *Schematic of PC setup*.

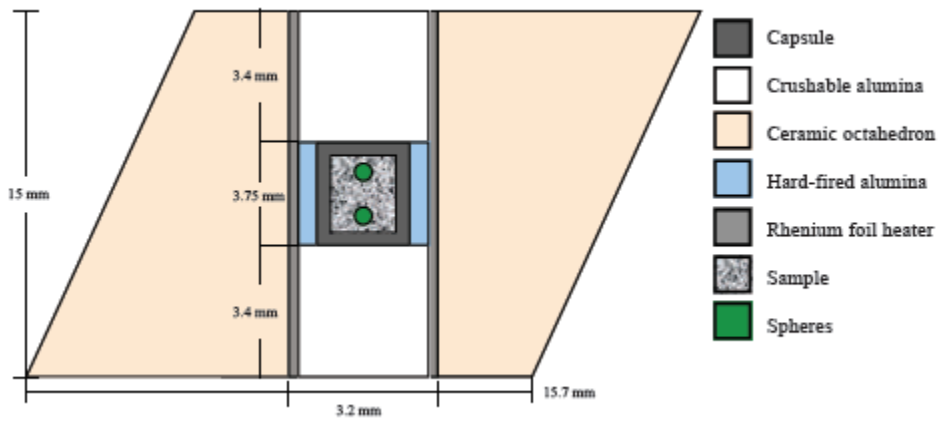

Figure A-2. *Schematic of MA setup.*

Calculation of Equilibrium Mineral Assemblages

First, the K_D values and equilibrium olivine compositions for each composition were calculated using the two models over the pressure range of the Moon. Calculation of K_D values from Toplis (2005) is given as (A1)

$$K_D{}^{Mg-Fe}_{Ol-Liq} = exp\left(\left[\frac{-6766}{RT} - \frac{7.34}{R}\right] + ln[0.036\%SiO_2\# - 0.22] + \left[\frac{3000(1-2X_{Fo})}{RT}\right] + 0.035P - 1RT \right) \quad \text{(A1)}$$

where R is the gas constant 8.31446 J/K*mol, T is temperature in Kelvin, X_{Fo} is mole fraction of forsterite in olivine (from 0-1), and P is pressure in bars. The molar silica content of the liquid is given by $\%SiO_2\#$ which is calculated from equations (A2-A5)

$$\%SiO_2\# = \%SiO_2^A + 0.8\ x\ wt\%H_2O \quad \text{(A2)}$$

in which $\%SiO_2^A$ is the adjusted silica content calculated by

$$\%SiO_2^A = \%SiO_2 + \Psi\ x\ (\%Na_2O + \%K_2O) \quad \text{(A3)}$$

where Ψ is defined as

$$\Psi = \left(0.46\left(\frac{100}{100-\%SiO_2}\right) - 0.93\right)(\%Na_2O + \%K_2O) + \left(-5.33\left(\frac{100}{100-\%SiO_2}\right) + 9.69\right) \quad (A4)$$

when $\%SiO_2 \leq 60$ mol% and Ψ is defined as

$$\Psi = \left(11 - 5.5\left(\frac{100}{100-\%SiO_2}\right)\right) \text{ x } \exp^{-0.13(\%Na_2O+\%K_2O)} \quad (A5)$$

when $\%SiO_2 > 60$ mol %. To determine the effect of pressure on the K_D values, we calculate K_D from Ulmer (1989) given as (13).

$$logK_D{}^{Ol-liq}_{Fe-Mg} = -0.5236(\pm 0.0028) + [P * 0.00378(\pm 0.00048)] - [P^2 * 1.81 \cdot$$

$$10{-}5(\pm 1.52{\cdot}10{-}5) \quad (A6)$$

where P is pressure in kbar. Equilibrium olivine compositions were determined from the K_D values calculated in each model at 2173 K (1900°C) (Figure A-3) as well as the temperature of the MSP for the different glasses.

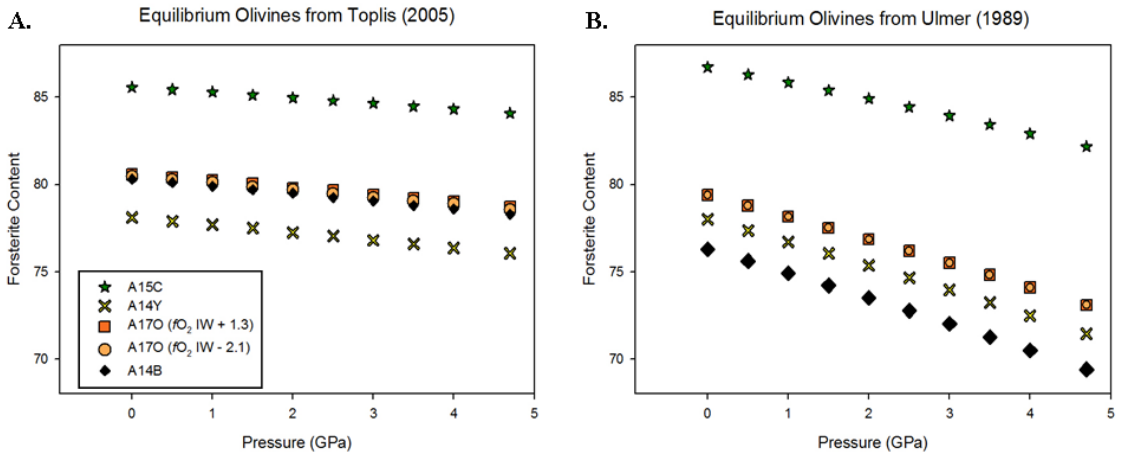

Figure A-3. *Equilibrium olivine compositions for lunar glasses.* **A.** Equilibrium olivine compositions calculated from the Toplis (2005) model. **B.** Equilibrium olivine compositions calculated from the Ulmer (1989) model. Note the larger range in compositions as a function of pressure, in B compared with A.

Next, the pyroxenes that would be in equilibrium with these olivines were calculated using the program QUILF (Andersen et al., 1993). This program considers the equilibrium relations of **Q**uartz, **U**lvospinel, **Il**menite and **F**ayalite given in equation (A7) to calculate equilibrium assemblages between various minerals.

$$SiO_2 + 2Fe_2TiO_4 = 2FeTiO_3 + Fe_2SiO_4 \quad \text{(A7)}$$

However, in most cases, the temperatures of interest were not within the limits of this calculator. Therefore, equilibrium pyroxenes were calculated over the temperature range of 673 K (400°C) to 1773 K (1500°C) at each pressure allowed by the calculator (1-3 GPa) and a logarithmic line was best fit to the data in order to allow us to extrapolate to the temperature in question. Following this, the compositions of the equilibrium pyroxenes for the temperature of interest (either 2173 K (1900°C) or the temperature of the MSP) were plotted as a function of pressure and a linear line was fit to the data in order to determine the equilibrium assemblage at the pressure ranges higher and lower than can be calculated using QUILF (i.e. 0-0.9 GPa and 3.1-4.7 GPa). The results of these calculations are shown in Figure A-4.

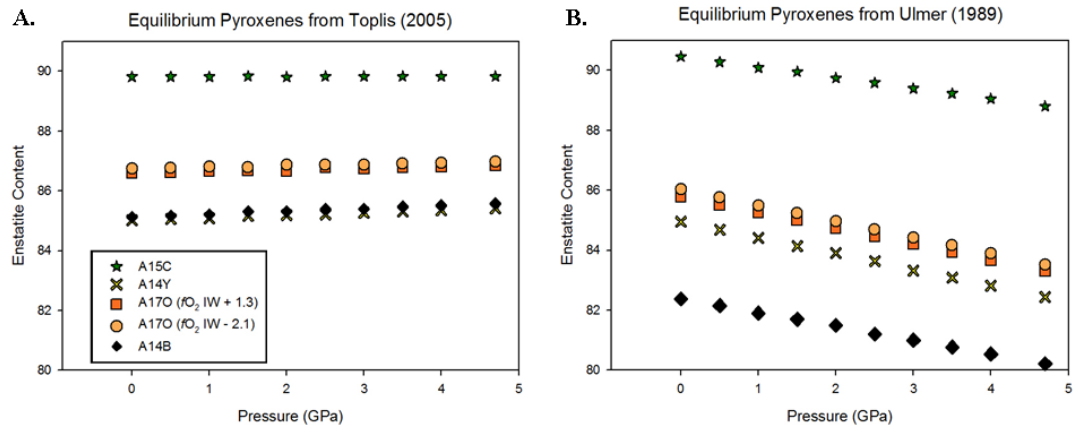

Figure A-4. *Equilibrium pyroxene compositions for lunar glasses.* **A.** Equilibrium pyroxene compositions calculated from the Toplis (2005) model. **B.** Equilibrium pyroxene compositions calculated from the Ulmer (1989) model. Again, note the larger range in compositions as a function of pressure, in B compared with A.

From here, the density of each equilibrium mineral was calculated at specified temperatures and pressures using the 3rd order Birch-Murnaghan equation of state (Eq. 1). These are the values plotted in the figures (e.g. Figure 3, 6, 9, 10, and 12) to determine where density crossovers occur between each melt and its equilibrium minerals (discussed in the results Section 3).

Appendix B-Experiments

This appendix contains a discussion of experimental difficulties we faced while attempting to constrain the density of the lunar glasses. Experimental run conditions for every experiment used in this study as well as BSE images of each experimental charge are shown here. Experimental run conditions for experiments resulting in near liquidus phases as well as EPMA analyses of these phases are also presented here.

Experimental Difficulties

As in any experimental study, throughout this research project many challenges were encountered. The most difficult part of running any sink-float experiment on a composition that does not have an established phase diagram up to the pressures of interest for the study is determining the temperature at any given pressure where the sample is entirely molten, but the density markers within it remain solid. Two extremes of problems can arise; either the entire sample does not melt, leaving near liquidus phase minerals and possible inhibiting the spheres from moving through the run (Figure B-1A), or the sample melts everything, including the spheres originally present (Figure B-1B). Although these results are not useful in bracketing the density of our compositions if the spheres remain in their original position, we can still get some data out of them. When liquidus phases are left over, the sample is still of use as we can construct a partial phase diagram for the composition (see results section 3). For the other extreme, when the sample and spheres are melted, we can use this as a data point to bracket the appropriate temperature for the given pressure of the experiment.

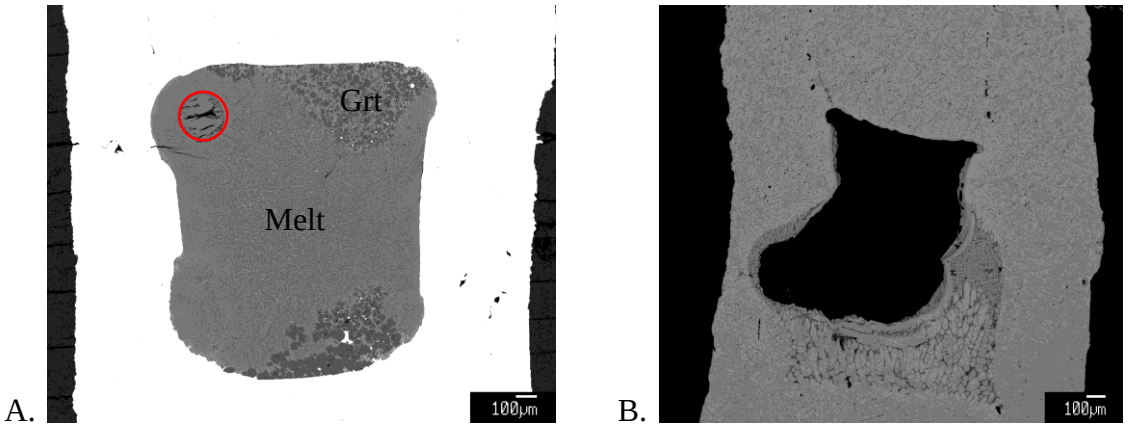

Figure B-1. *Difficulty in determining experimental T.* **A**. Sample GG-KV-13. This experiment at 9 GPa and 2423 K(2150°C) did not melt completely, leaving liquidus phase garnets behind at the top and bottom of the capsule. The red circle outlines the top sphere. **B.** Sample OG-KV-22 This experiment at 11GPa and 2473K (2200°C) melted the entirety of the starting material as well as the two spheres placed in the capsule initially. Contrast was increased in the image to show the Fe-metal formed during the experiment. Both images are backscattered electron images (BSE).

Another obstacle in determining the correct temperature of the starting composition at a given pressure arises from the high FeO content in the lunar glasses. For the green, yellow, and orange lunar glasses, the FeO contents are 16.5 wt%, 24.7 wt%, and 22.9 wt%, respectively. Due to the picritic nature of these glasses, higher temperatures are needed to melt the starting composition. However, at these higher temperatures there is a reaction that takes place between the iron in the starting material and the molybdenum metal of the capsule (eq. B1):

$$Mo^{metal} + 2FeO^{melt} \longleftrightarrow MoO_2^{melt} + 2Fe^{metal} \quad \text{(B1)}$$

This reaction causes the iron in the starting material to be extracted from the melt as iron metal and molybdenum to be introduced into the silicate melt as MoO_2 species (Figure B-1B above and Figure B-2 below). This reaction proceeds until the oxygen fugacity of the experiment is close to that of the Mo-MoO_2 buffer. As a result, the final composition of the melt in which the spheres sink or float is driven from the starting composition of the melt creating an uncertainty in the density of the composition of interest. Therefore, a

correction has to be made each time the temperature is high enough that the reaction in equation B1 takes place. This is done by determining the 1-bar density of the ideal melt (starting composition) at the temperature of the experiment and the 1-bar density of the melt analyzed by EPMA at the same temperature. Assuming a linear relationships at high pressures, the density of the melt is corrected by the difference in the 1-bar densities of the ideal and actual melt compositions. This takes into account any MoO_2 addition into the run as well as any FeO loss.

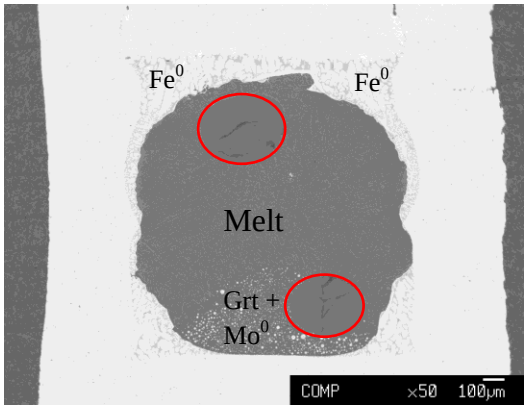

Figure B-2. *Difficulty with high FeO content of lunar glasses.* Sample YG-KV-11 at 9.5 GPa and 2473 K (2200°C). Due to the high FeO content of this melt molybdenum metal was introduced into the sample and iron metal was extracted. However, as shown by the garnet crystals present at the bottom of the sample, the bottom sphere was unable to move during the 30 second run duration resulting in a false neutral buoyancy. The red circles outline the spheres.

The final difficulty during the experimental procedures of this project only affected the green glass portion of the study. As seen from the bulk composition of A15C (Table 1), this glass has a high Mg# of ~66. As discussed previously, for the lower pressure experiments, forsterite-rich olivines are used to bracket the density of the melt. Low pressure data for the green glass were bracketed with Fo_{100} spheres by Smith and Agee (1997). However, we were not able to reproduce these results during this study. The main challenge with using forsterite-rich spheres as density markers is the optical

similarity between the melt and the mineral, both having high Mg#'s. Figure B-3A shows an experimental charge at 3.0 GPa and 2048 K (1775°C) in reflected light of a polarizing microscope. As seen in the image, the sphere is almost indistinguishable from the melt down to a 0.3µm polish. Figure B-3B shows the same experimental charge in backscatter electron view from the electron probe. The mineral density marker is outlined in red. Although the sphere is visible, this is not the view we have throughout the grinding and polishing steps discussed in section 2.3. As a result, multiple forsterite-rich spheres were most likely ground through at these lower pressures and our experimental data, although well constrained with previously published low pressure data, is only for higher pressures outside of the pressure range of the Moon.

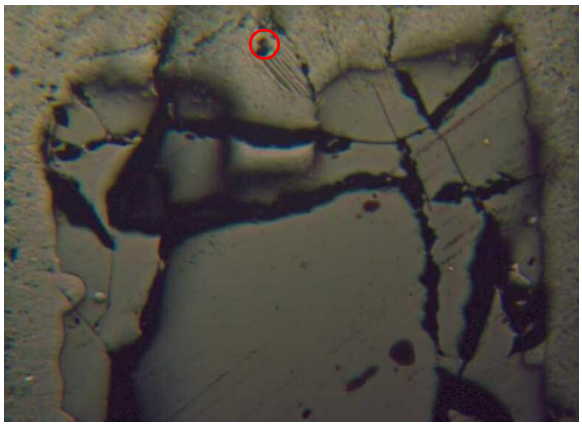

A.

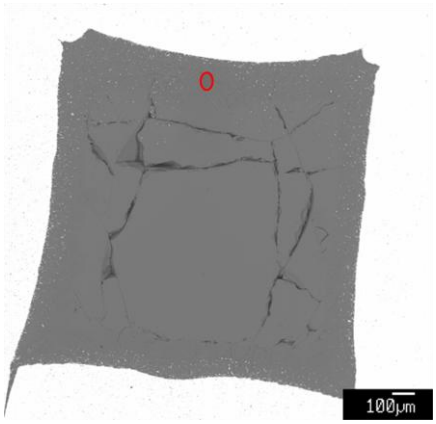

B.

Figure B-3. *Difficulty resulting from optical similarities between melt and density markers.* **A**. Sample GG-KV-18 at 3.0 GPa and 2048 K (1775°C) reflected light image. Sphere is outlined in red. **B.** BSE image of the same sample with the mineral density marker outlined in red. As a result of the optical similarity between the olivine spheres and the green glass melt, we were not able to place further constraints on the density of this composition at lower pressures.

Experimental Results

Table B-1. *Experimental run conditions, sink/float results, and melt compositions for A15C.* This Table gives the experimental run number, the sphere used in the experiment, the pressure and temperature of the experiment, and the experimental result. Also given is the average EPMA totals and oxide wt %'s, the density of the liquid from the experimental charge at the PT conditions of the experiment (ρ_{liq}), the density of the ideal liquid at the PT conditions of the experiment ($\rho_{ideal\ liq}$), the density of the sphere itself (ρ_{sphere}) and the calculated densities for 2173 K (1900°C) and the MSP temperature of the composition.

Run	GG-KV-11	GG-KV-14	GG-KV-17	GG-KV-19
Sphere	$Py_{49}Al_{31}Gr_{18}Sp_1$	$Py_{49}Al_{31}Gr_{18}Sp_1$	$Py_{49}Al_{31}Gr_{18}Sp_1$	$Py_{63}Al_{24}Gr_{12}Sp_1$
P(GPa)	7	9	7.5	8.5
T(K)	2323	2473	2373	2448
Result	Sink	Float	Sink	Sink
SiO_2	49.86	51.04	51.52	52.23
TiO_2	0.29	0.29	0.28	0.31
Al_2O_3	6.73	8.19	7.86	7.17
Cr_2O_3	0.50	0.56	0.54	0.53
FeO	15.23	12.12	12.95	11.93
MgO	18.10	18.53	18.14	18.15
MnO	0.23	0.26	0.24	0.25
CaO	8.39	8.35	8.26	8.66
Na_2O	0.10	0.09	0.09	0.10
K_2O	0.10	0.08	0.08	0.09
MoO_2	1.78	1.33	1.43	1.44
Total	101.31	100.84	101.39	100.87
ρ_{liq}	2.68	2.61	2.64	2.61
$\rho_{ideal\ liq}$	2.69	2.66	2.68	2.67
ρ_{sphere}	3.73	3.77	3.74	3.74
$\rho_{ideal2173K}$	2.72	2.72	2.72	2.72
$\rho_{sphere2173K}$	3.78	3.93	3.87	3.91
$\rho_{ideal1793K}$	2.79	2.79	2.79	2.79
$\rho_{sphere1793K}$	3.85	4.00	3.94	3.98

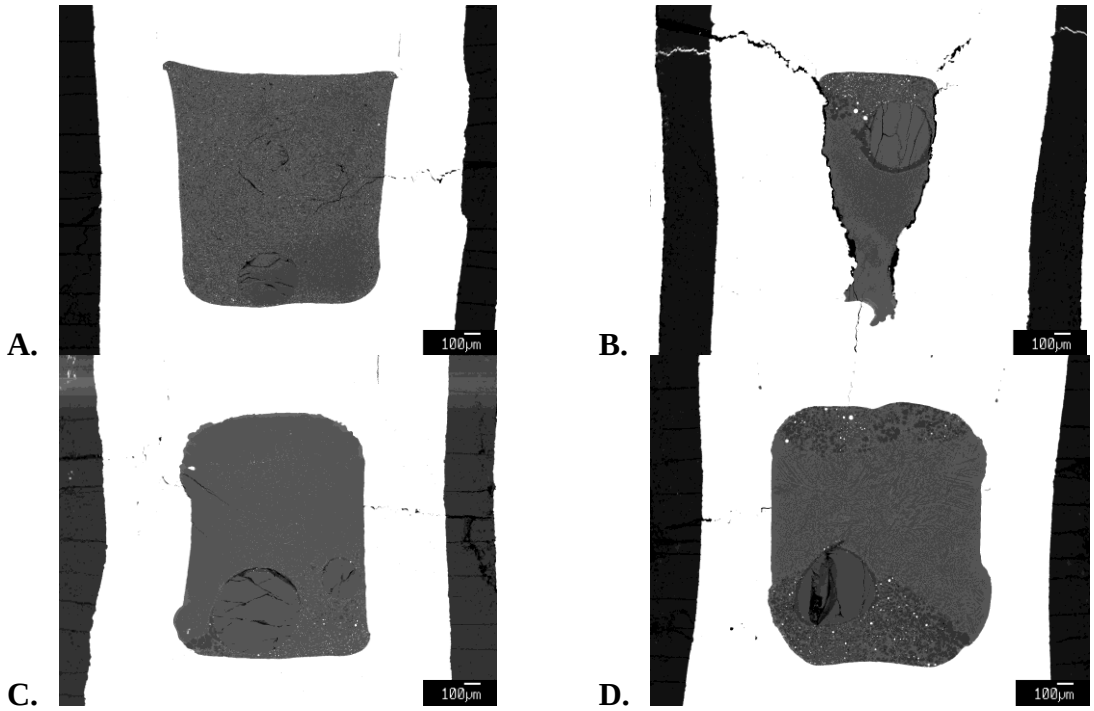

Figure B-4. *BSE images of experimental charges for A15C*. **A.**GG-KV-11 **B.** GG-KV-14 **C.** GG-KV-17 **D.** GG-KV-19 All images have magnification of X 45 and show a 100 µm scale bar in the lower right hand corner. The top of every image corresponds to the top of the capsule during the experiment.

Table B-2. *Experimental run conditions, sink/float results, and melt compositions for A14Y.* This Table gives the experimental run number, the sphere used in the experiment, the pressure and temperature of the experiment, and the experimental result. Also given is the average EPMA totals and oxide wt %'s, the density of the liquid from the experimental charge at the PT conditions of the experiment (ρ_{liq}), the density of the ideal liquid at the PT conditions of the experiment ($\rho_{ideal\ liq}$), the density of the sphere itself (ρ_{sphere}) and the calculated densities for 2173 K (1900°C) and the MSP temperature of the composition.

Yellow Glass											
Run	**YG-KV-4**	**YG-KV-7**	**YG-KV-8**	**YG-KV-14**	**YG-KV-15**	**YG-KV-16**	**YG-KV-17**	**YG-KV-19**	**YG-KV-20**	**YG-KV-22**	**YG-KV-27**
Sphere	Fo_{100}	Fo_{100}	Fo_{90}	Fo_{100}	Fo_{83}	Fo_{90}	Fo_{83}	Fo_{100}	Fo_{90}	$Py_{67}Al_{12}Gr_5Sp_{16}$	$Py_{67}Al_{12}Gr_4Sp_{17}$
P(GPa)	1	3	3	2.5	3	1.5	4	1.5	2.5	6	7.5
T(K)	1748	2048	2048	2023	1973	1803	2023	1803	1948	2248	2423
Result	Sink	Float	Float	Float	Sink	Sink	Float	Sink	Neutral	Sink	Neutral
SiO_2	41.78	40.61	41.95	41.52	42.22	41.48	41.77	41.59	41.21	43.50	44.88
TiO_2	4.29	4.01	4.09	4.26	3.87	4.23	3.90	4.24	4.12	4.27	4.61
Al_2O_3	6.55	6.01	6.28	6.30	5.98	6.36	5.99	6.40	6.09	6.55	7.69
Cr_2O_3	0.38	0.36	0.37	0.38	0.37	0.37	0.37	0.38	0.38	0.37	0.40
FeO	23.72	24.09	22.87	22.61	23.77	24.57	22.79	23.18	23.50	20.66	15.99
MgO	15.60	15.12	16.64	16.80	16.86	15.56	17.45	16.43	16.37	15.34	16.36
MnO	0.30	0.31	0.30	0.31	0.31	0.31	0.31	0.31	0.30	0.41	0.59
CaO	6.86	6.71	6.72	6.82	6.38	6.92	6.55	6.80	6.66	7.35	6.62
Na_2O	0.39	0.41	0.43	0.41	0.39	0.44	0.38	0.43	0.42	0.51	0.51
K_2O	0.09	0.12	0.09	0.10	0.08	0.10	0.11	0.11	0.10	0.09	0.08
MoO_2	0.78	4.00	1.27	1.27	0.56	0.75	1.52	0.72	0.96	2.57	1.86
Total	100.75	101.76	101.01	100.77	100.78	101.09	101.15	100.59	100.11	101.61	99.59
ρ_{liq}	2.95	2.92	2.87	2.88	2.89	2.95	2.88	2.93	2.91	2.80	2.69
$\rho_{ideal\ liq}$	2.96	2.89	2.89	2.89	2.90	2.95	2.89	2.95	2.91	2.84	2.79
ρ_{sphere}	3.07	3.05	3.18	3.05	3.28	3.19	3.29	3.07	3.19	3.70	3.72
$\rho_{ideal1900c}$	2.85	2.85	2.85	2.85	2.85	2.85	2.85	2.85	2.85	2.85	2.85
$\rho_{sphere1900c}$	2.98	2.95	3.18	3.04	3.26	3.10	3.27	3.00	3.14	3.80	3.99
$\rho_{ideal1550c}$	2.94	2.94	2.94	2.94	2.94	2.94	2.94	2.94	2.94	2.94	2.94
$\rho_{sphere1550c}$	3.07	3.04	3.27	3.13	3.35	3.19	3.36	3.09	3.23	3.89	4.08

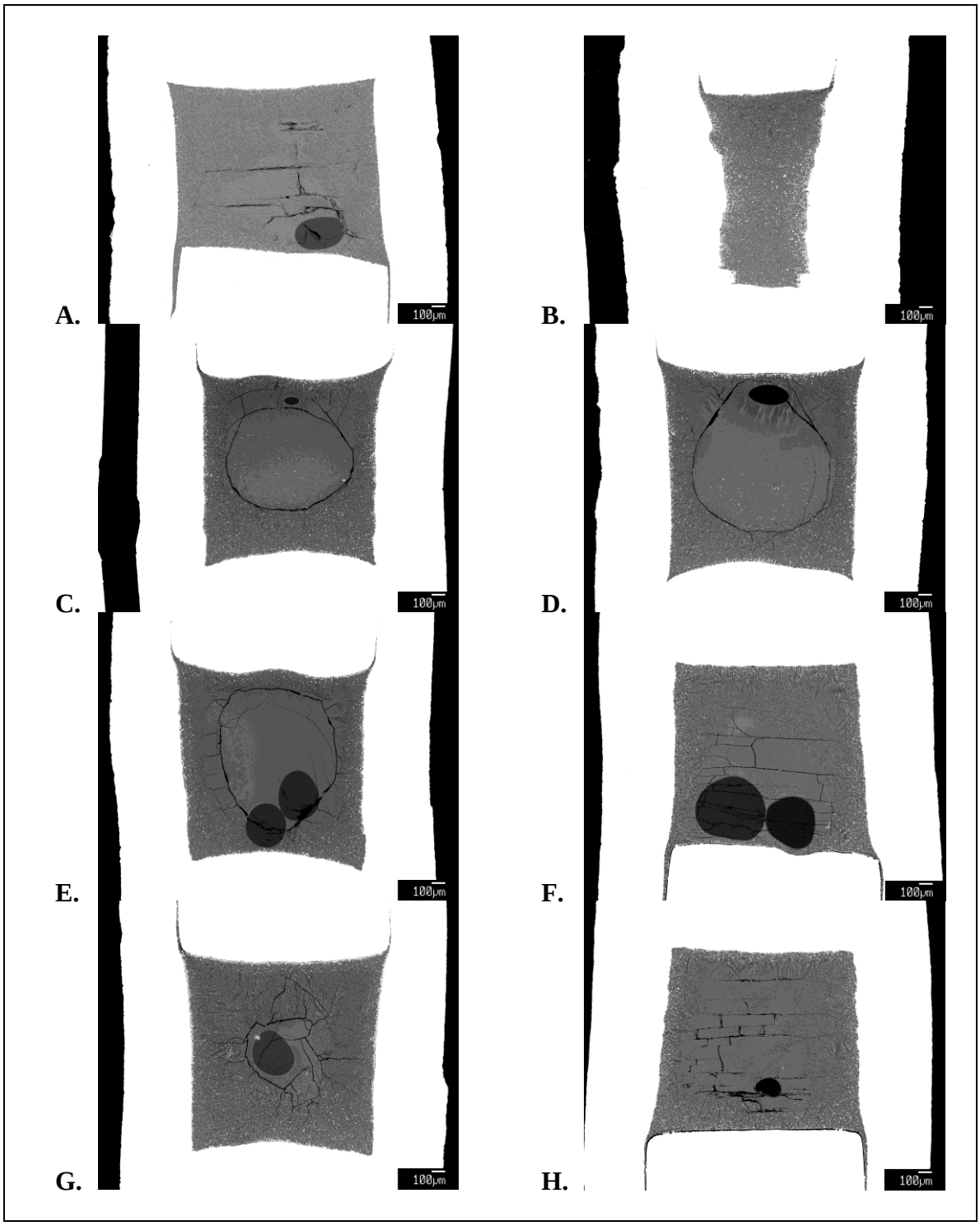
A.
B.
C.
D.
E.
F.
G.
H.
100µm

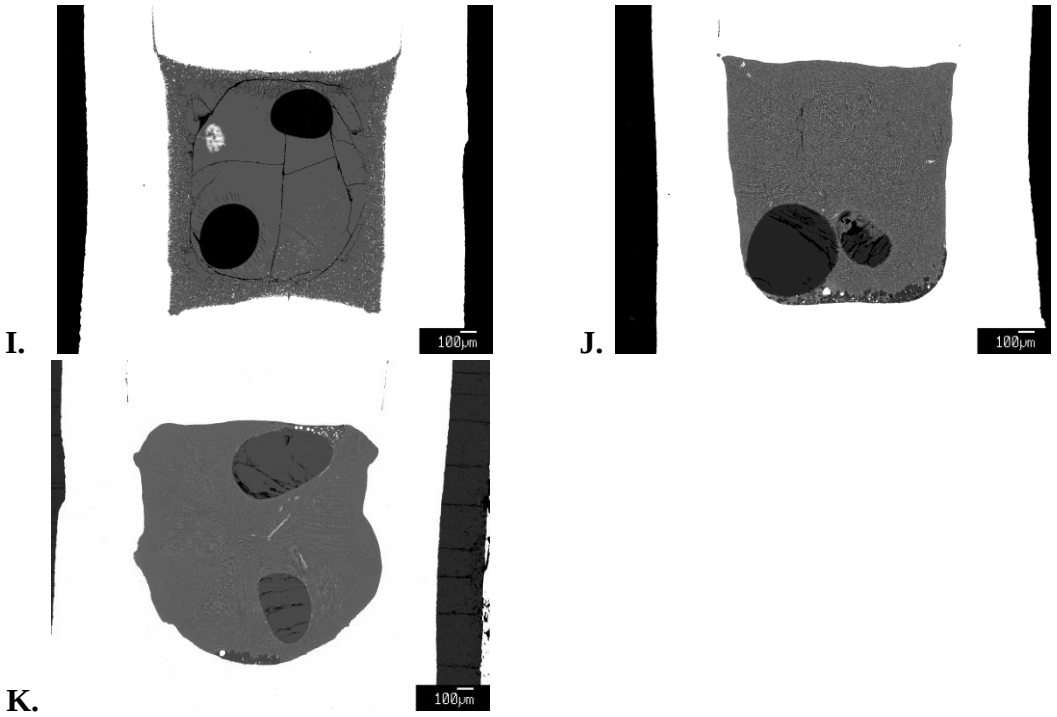

Figure B-5. *BSE images of experimental charges for A14Y*. **A.** YG-KV-4 **B.** YG-KV-7 **C.** YG-KV-8 **D.** YG-KV-14 **E.** YG-KV-15 **F.** YG-KV-16 **G.** YG-KV-17 **H.** YG-KV-19 **I.** YG-KV-20 **J.** YG-KV-22 **K.** YG-KV-27 All images have magnification of X 45 and show a 100 µm scale bar in the lower right hand corner. The top of every image corresponds to the top of the capsule during the experiment. Decompression cracks are seen in some of the images.

Table B-3. *Experimental run conditions, sink/float results, and melt compositions for A17O.* This Table gives the experimental run number, the sphere used in the experiment, the pressure and temperature of the experiment, and the experimental result. Also given is the average EPMA totals and oxide wt %'s, the density of the liquid from the experimental charge at the PT conditions of the experiment (ρ_{liq}), the density of the ideal liquid at the PT conditions of the experiment ($\rho_{ideal\ liq}$), the density of the sphere itself (ρ_{sphere}) and the calculated densities for 2173 K (1900°C) and the MSP temperature of the composition.

Orange Glass				
Run	**OG-KV-1**	**OG-KV-5**	**OG-KV-20**	**OG-KV-23**
Sphere	$Py_{60}Al_{37}Gr_3$	$Py_{60}Al_{37}Gr_3$	$Py_{34}Al_{57}Gr_5Sp_4$	$Py_{49}Al_{31}Gr_{18}Sp_1$
P(GPa)	6.9	8	8	10
T(K)	2173	2223	2373	2423
Result	Neutral	Float	Sink	Sink
SiO_2	39.43	39.71	40.77	42.80
TiO_2	8.61	7.92	9.07	9.18
Al_2O_3	6.50	6.82	6.23	6.62
Cr_2O_3	0.71	0.71	0.67	0.71
FeO	20.87	19.65	17.93	15.11
MgO	15.32	16.49	15.56	16.47
MnO	0.29	0.28	0.34	0.32
CaO	7.55	7.40	7.72	7.72
Na_2O	0.33	0.32	0.33	0.34
K_2O	0.04	0.04	0.04	0.04
MoO_2	2.09	2.12	2.63	2.28
Total	101.75	101.46	101.30	101.59
ρ_{liq}	2.85	2.82	2.79	2.71
$\rho_{ideal\ liq}$	2.86	2.85	2.81	2.79
ρ_{sphere}	3.81	3.83	4.01	3.83
$\rho_{ideal2173K}$	2.86	2.86	2.86	2.86
$\rho_{sphere2173K}$	3.83	3.89	4.10	4.07
$\rho_{ideal1803K}$	2.97	2.97	2.97	2.97
$\rho_{sphere1803K}$	3.94	4.00	4.21	4.18
$\rho_{ideal1833K}$	2.96	2.96	2.96	2.96
$\rho_{sphere1833K}$	3.93	3.99	4.20	4.17

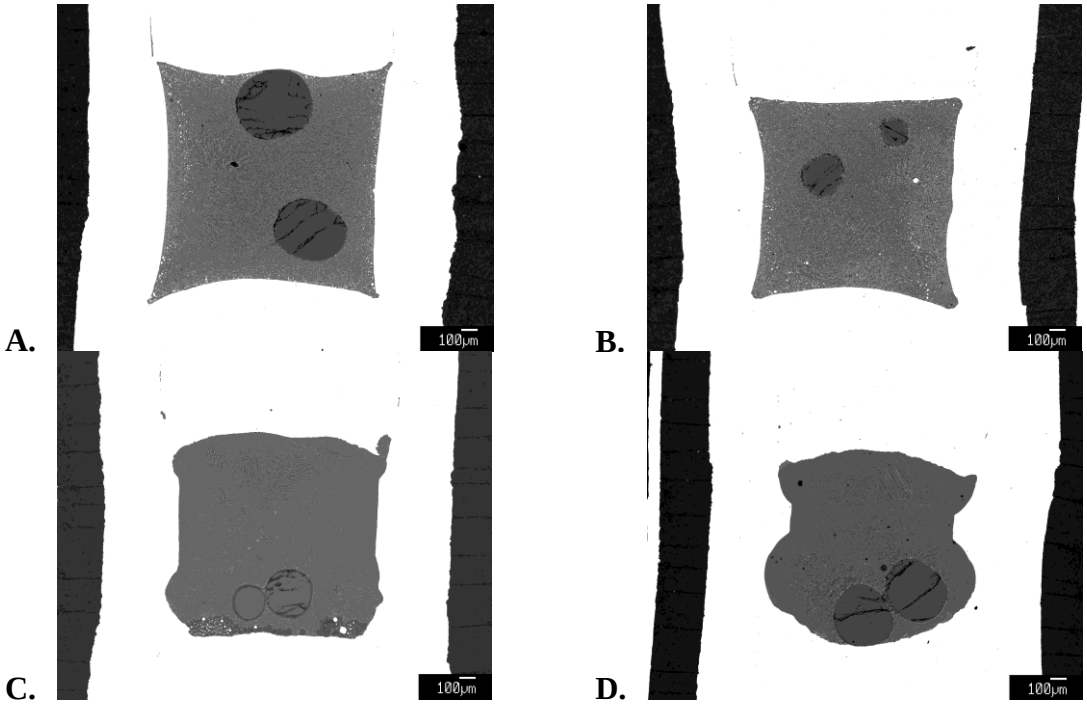

Figure B-6. *BSE images of experimental charges for A17O*. **A.** OG-KV-1 **B.** OG-KV-5 **C.** OG-KV-20**D.** OG-KV-23. All images have magnification of X 45 and show a 100 µm scale bar in the lower right hand corner. The top of every image corresponds to the top of the capsule during the experiment.

Table B-4.1. *PC experimental run conditions, sink/float results, and melt compositions for A14B with corrected densities for temperatures of interest.* This Table gives the experimental run number, the sphere used in the experiment, the pressure and temperature of the experiment, and the experimental result for all PC experiments on this composition. Also given is the average EPMA totals and oxide wt %'s, the density of the liquid from the experimental charge at the PT conditions of the experiment (ρ_{liq}), the density of the ideal liquid at the PT conditions of the experiment ($\rho_{ideal\ liq}$), the density of the sphere itself (ρ_{sphere}) and the calculated densities for 2173 K (1900°C) and the MSP temperature of the composition.

Run	67PC	64PC	63PC	62PC	88PC	84PC
Sphere	Fo_{90}	Fo_{90}	Fo_{90}	Fo_{90}	$Fo_{84.3}$	$Fo_{84.3}$
P(GPa)	1	1.5	2	2.5	1.5	2
T(K)	1688	1708	1738	1758	1707	1738
Result	Float	Float	Float	Float	neutral	Float
SiO_2	34.62	34.26	33.69	34.22	34.29	34.32
TiO_2	15.03	15.63	15.36	15.74	15.23	15.40
Al_2O_3	4.71	4.74	4.73	4.77	4.74	4.74
Cr_2O_3	0.67	0.92	0.92	1.00	0.75	0.81
FeO	22.79	22.86	23.19	22.01	22.73	22.64
MgO	14.00	14.38	13.88	14.84	14.19	14.25
CaO	6.67	6.41	6.49	6.35	6.56	6.60
$MoO_{3(2)}$	1.88	1.55	2.18	2.35	1.84	2.00
Total	100.37	100.75	100.44	101.28	100.33	100.76
ρ_{liq}	3.09	3.09	3.09	3.07	3.09	3.08
$\rho_{ideal\ liq}$	3.09	3.08	3.07	3.06	3.08	3.07
ρ_{sphere}	3.22	3.23	3.25	3.26	3.30	3.31
$\rho_{ideal2173K}$	2.92	2.92	2.92	2.92	2.92	2.92
$\rho_{sphere2173K}$	3.05	3.05	3.06	3.10	3.12	3.14
$\rho_{ideal1703K}$	3.09	3.09	3.09	3.09	3.09	3.09
$\rho_{sphere1703K}$	3.22	3.22	3.23	3.27	3.29	3.31

Table B-4.2. *Experimental MA run conditions, sink/float results, and melt compositions for A14B with corrected densities for temperatures of interest.* This Table gives the experimental run number, the sphere used in the experiment, the pressure and temperature of the experiment, and the experimental result. Also given is the average EPMA totals and oxide wt %'s, the density of the liquid from the experimental charge at the PT conditions of the experiment (ρ_{liq}), the density of the ideal liquid at the PT conditions of the experiment ($\rho_{ideal\ liq}$), the density of the sphere itself (ρ_{sphere}) and the calculated densities for 2173 K (1900°C) and the MSP temperature of the composition.

Run	301A8	308A8	321A8	310A8	401A8	402A8	405A8	410A8
Sphere	$Py_{69.7}Al_{17}Gr_{13.3}$	$Py_{69.7}Al_{17}Gr_{13.3}$	$Py_{69.7}Al_{17}Gr_{13.3}$	$Py_{69.7}Al_{17}Gr_{13.3}$	$Py_{69.7}Al_{17}Gr_{13.3}$	$Py_{63.0}Al_{28.7}Gr_{8.3}$	$Py_{63.0}Al_{28.7}Gr_{8.3}$	$Py_{63.0}Al_{28.7}Gr_{8.3}$
P(GPa)	4	5	5.5	6	6	8.2	8.5	9
T(K)	1983	2048	2073	2077	2108	2238	2258	2283
Result	Sink	Sink	Neutral	Float	Neutral	Sink	Sink	Sink
SiO_2	34.64	34.44	33.47	34.53	34.85	32.72	33.39	34.09
TiO_2	15.10	14.72	15.09	14.61	14.45	15.95	15.38	14.97
Al_2O_3	3.81	4.43	4.91	3.89	5.13	3.78	4.49	4.85
Cr_2O_3	0.69	0.83	0.88	0.79	0.87	0.76	0.83	0.91
FeO	23.03	22.44	22.30	22.04	22.12	23.65	22.69	21.67
MgO	14.29	14.32	13.99	14.31	14.43	13.11	13.44	13.90
CaO	6.75	6.64	6.53	6.79	6.70	6.54	6.56	6.75
$MoO_{3(2)}$	3.17	3.60	3.84	4.30	2.75	3.81	3.74	3.77
Total	101.48	101.42	101.01	101.26	101.30	100.32	100.52	100.91
ρ_{liq}	3.01	2.99	2.99	2.98	2.95	2.96	2.93	2.91
$\rho_{ideal\ liq}$	2.98	2.96	2.95	2.95	2.94	2.90	2.89	2.89
ρ_{sphere}	3.62	3.64	3.65	3.66	3.66	3.79	3.80	3.81
$\rho_{ideal2173K}$	2.92	2.92	2.92	2.92	2.92	2.92	2.92	2.92
$\rho_{sphere2173K}$	3.50	3.54	3.54	3.57	3.62	3.69	3.75	3.80
$\rho_{ideal1703K}$	3.09	3.09	3.09	3.09	3.09	3.09	3.09	3.09
$\rho_{sphere1703K}$	3.67	3.71	3.71	3.74	3.79	3.86	3.92	3.97

Table B-4.3. *Experimental MA run conditions, sink/float results, and melt compositions for A14B with corrected densities for temperatures of interest.* This Table gives the experimental run number, the sphere used in the experiment, the pressure and temperature of the experiment, and the experimental result. Also given is the average EPMA totals and oxide wt %'s, the density of the liquid from the experimental charge at the PT conditions of the experiment (ρ_{liq}), the density of the ideal liquid at the PT conditions of the experiment ($\rho_{ideal\ liq}$), the density of the sphere itself (ρ_{sphere}) and the calculated densities for 2173 K (1900°C) and the MSP temperature of the composition.

Run	426A8	455A8	397A8	399A8	412A8	390A8	411A8
Sphere	$Py_{63.0}Al_{28.7}Gr_{8.3}$	$Py_{63.0}Al_{28.7}Gr_{8.3}$	$Py_{61.4}Al_{35.9}Gr_{2.7}$	$Py_{61.4}Al_{35.9}Gr_{2.7}$	$Py_{61.4}Al_{35.9}Gr_{2.7}$	$Py_{61.4}Al_{35.9}Gr_{2.7}$	$Py_{61.4}Al_{35.9}Gr_{2.7}$
P(GPa)	10	11.5	8.8	9.2	10	9.4	10
T(K)	2328	2353	2268	2283	2333	2293	2348
Result	Neutral	Neutral	Sink	Sink	Sink	Sink	Sink
SiO_2	34.27	35.50	33.93	34.05	33.57	33.83	35.06
TiO_2	14.15	17.20	14.92	14.84	15.08	15.59	15.56
Al_2O_3	5.95	4.55	5.08	5.65	4.96	5.20	6.30
Cr_2O_3	0.93	0.87	0.85	0.84	0.91	0.87	0.93
FeO	21.54	17.71	21.96	20.87	22.00	20.72	17.85
MgO	14.05	14.32	13.80	14.06	13.78	13.78	14.28
CaO	6.49	7.05	6.60	6.44	6.58	6.51	6.86
$MoO_{3(2)}$	3.50	3.40	3.61	3.85	3.88	4.13	3.53
Total	100.88	100.60	100.75	100.60	100.76	100.63	100.37
ρ_{liq}	2.88	2.83	2.91	2.90	2.90	2.90	2.83
$\rho_{ideal\ liq}$	2.87	2.86	2.89	2.89	2.87	2.88	2.86
ρ_{sphere}	3.83	3.86	3.85	3.86	3.88	3.95	3.95
$\rho_{ideal2173K}$	2.92	2.92	2.92	2.92	2.92	2.92	2.92
$\rho_{sphere2173K}$	3.86	3.98	3.84	3.87	3.87	3.95	4.07
$\rho_{ideal1703K}$	3.09	3.09	3.09	3.09	3.09	3.09	3.09
$\rho_{sphere1703K}$	4.03	4.15	4.01	4.04	4.04	4.12	4.24

Table B-5. *Garnet compositions in near liquidus runs.* This Table gives garnet compositions for the experimental runs that resulted in near-liquidus assemblages. Graphical representation of the green glass and yellow glass results are given in Figure 4 and Figure 7, respectively.

Glass	Green	Green	Green	Green	Yellow	Yellow	Yellow	Yellow	Orange	Orange
Run	GG-KV-13	GG-KV-14	GG-KV-17	GG-KV-19	YG-KV-18	YG-KV-22	YG-KV-24	YG-KV-25	OG-KV-19	OG-KV-20
P(GPa)	9	9	7.5	8.5	6	6	7.5	8.5	6	8
T(K)	2423	2473	2373	2448	2148	2248	2348	2373	2273	2373
Composition of Crystals										
SiO_2	46.68	45.82	45.97	46.21	54.71	43.78	45.65	45.37	43.61	43.73
TiO_2	0.11	0.07	0.07	0.10	0.41	1.53	1.36	1.40	2.43	2.50
Al_2O_3	17.97	18.98	19.70	18.32	2.31	19.15	18.06	18.24	18.86	18.48
Cr_2O_3	0.74	0.74	0.76	0.68	0.24	0.77	0.64	0.64	1.17	1.04
FeO	7.29	7.07	7.83	7.07	11.47	11.19	10.57	10.26	10.08	8.95
MgO	23.49	23.23	22.13	23.04	21.07	19.56	20.21	20.15	19.24	21.12
MnO	0.23	0.22	0.22	0.22	0.23	0.33	0.31	0.31	0.25	0.29
CaO	4.88	4.47	4.52	4.79	9.85	4.88	5.22	5.13	5.50	5.42
Na_2O	0.02	0.03	0.03	0.04	0.81	0.07	0.12	0.13	0.08	0.09
K_2O	0.03	0.02	0.03	0.03	0.03	0.03	0.02	0.02	0.02	0.02
MoO_2	0.21	0.11	0.17	0.18	0.03	0.29	0.20	0.15	0.29	0.34
Total	101.64	100.76	101.42	100.67	101.17	101.57	102.37	101.80	101.53	101.99
Pyrope	75.25	76.07	74.02	75.37	60.70	66.25	67.22	67.68	66.37	69.93
Almandine	13.11	12.98	14.68	12.97	18.54	21.25	19.71	19.33	19.50	16.62
Grossular	11.23	10.53	10.87	11.25	20.39	11.87	12.47	12.39	13.63	12.90
Spessartine	0.42	0.42	0.43	0.42	0.37	0.63	0.59	0.59	0.49	0.55

References

Agee, C. B. (1998) Crystal-liquid density inversions in terrestrial and lunar magmas. *Physics of the Earth and Planetary Interiors* **107**, 63-74.

Agee, C.B. (2008) Static compression of hydrous silicate melt and the effect of water on planetary differentiation. *Earth Planet Sci. Lett,* **265**, 641-654.

Agee C. B. and Walker, D. (1988) Static compression and olivine flotation in ultrabasic silicate liquid. *Journal of Geophysical Research Solid Earth Planets,* **93**, 3437-3449.

Agee C. B. and Walker, D. (1993) Olivine flotation in mantle melt. *Earth Planet Sci. Lett,* **114**, 315-324.

Anderson, D.J., Lindsley, D.H., and Davidson, P.M. (1993) QUILF: A pascal program to assess equilibria among Fe-Mg-Mn-Ti oxides, pyroxenes, olivine, and quartz. *Computers & Geosciences,* **19,** 1333-1350.

Asimow, P.D., and Longhi, J. (2004) The significance of multiple saturation points in the context of polybaric near-fractional melting. *Journal of Petrology*, **45,** 2349-2367.

Boyce, J.W., Liu, Y., Rossman, F.R., Guan, Y., Eiler, J.M., Stolper, E.M., and Taylor, L.A. (2010) Lunar apatite with terrestrial volatile abundances. *Nature*, **466**, 466-470.

Circone S. and Agee, C.B. (1996) Compressibility of molten high-Ti mare glass: evidence for crystal-liquid density inversions in the lunar mantle. *Geochim. Cosmochim. Acta*, **60**, 2709-2720.

Conrad P. G., Zha C. S., Mao, H. K., and Hemley, R. J. (1999) The high-pressure, single-crystal elasticity of pyrope, grossular, and andradite. *American Mineralogist*, **84,** 374-383.

Delano, J. W. (1979) Apollo 15 green glass: Chemistry and possible origin. *Proc. Lunar Planet. Sci. Conf.,* **10**, 275-300.

Delano, J. W. (1986) Pristine lunar glasses: Criteria, data, and implications. *Proc. Lunar Planet. Sci. Conf.,* **17**, D201-D213.

Delano, J. W. (1990) Buoyancy-driven melt segregation in earth's moon: 1. Numerical results. *Proc. 20th Lunar Planet. Sci. Conf.,* 3-12.

De Vries, J., van den Berg, A., and van Westrenen, W. (2010) Formation and evolution of a lunar core from ilmenite-rich magma ocean cumulates. *Earth and Planetary Science Letters*, **292,** 139-147.

Draper, D.S., duFrane, S.A., Shearer, C.K., Dwarzski, R.E., and Agee, C.B. (2006) High-pressure phase equilibria and element partitioning experiments on Apollo 15 green C picritic glass: Implications for the role of garnet in the deep lunar interior. *Geochim. Cosmochim. Acta*, **70**, 2400-2416.

Elardo, S.M., Draper, D.S., and Shearer, C.K. Jr. (2011) Lunar Magma Ocean crystallization revisited: Bulk composition, early cumulate mineralogy, and the source regions of the highlands Mg-suite. *Geochim. Cosmochim. Acta*, **75**, 3024-3045.

Elkins-Tanton, L.T., Chatterjee, N., and Grove, T.L. (2003a) Experimental and petrological constraints on lunar differentiation from the Apollo 15 green picritic glasses. *Meteoritics & Planetary Science*, **38,** Nr 4. 515-527.

Elkins-Tanton, L.T., Chatterjee, N., and Grove, T.L. (2003b) Magmatic processes that produced lunar fire fountains. *Geophysical Research Letters*, **30**(10), 1513.

Elkins-Tanton, L.T. and Grove, T.L. (2011) Water (hydrogen) in the lunar mantle: Results from petrology and magma ocean modeling. *Earth and Planetary Science Letters*, **307,** 173-179.

Elkins-Tanton, L.T. Burgess, S., and Yin, Q.Z. (2011) The lunar magma ocean: Reconciling the solidification process with lunar petrology and geochronology. *Earth and Planetary Science Letters*, **307,** 326-336.

Farges, F. and Brown, G. E. Jr. (1997) Coordination chemistry of titanium (IV) in silicate glasses and melts: IV. XANES studies of synthetic and natural volcanic glasses and tektites at ambient temperature and pressure. *Geochim. Cosmochim. Acta*, **61**, 1863-1870.

Fegley, B. and Swindle, T.D. (1993) Lunar volatiles: Implications for lunar resource utilization. *In* Resources of Near-Earth Space. Lewis J, Matthews, MS, Guerrieri ML (eds), Univ Arizona Press, Tucson, 367-426.

Fogel, R.A. and Rutherford, M.J. (1995) Magmatic volatiles in primitive lunar glasses: FTIR and EMPA analyses of Apollo 15 green and yellow glasses and revisions of the volatile assisted fire-fountaining theory. *Geochim Cosmochim. Acta*, **59,** 201-215.

Fukui, H., Kanzaki, M., Hiraoka, N., and Cai, Y.Q. (2008) Coordination environment of silicon in silica glass up to 74 GPa: An x-ray Raman scattering study at the silicon L edge, *Physical Review B*, **78,** 012203-1-012203-4.

Ghiorso M. S. and Kress, V. C. (2004) An equation of state for silicate melts. II: Calibration of volumetric properties at 10^5 Pa. *Am. J. Sci.* **304,** 679-751.

Goto, T., Anderson, O. L., Ohno, I., Yamamoto, S. (1989) Elastic constants of corundum up to 1825 K. *J. Geophys. Res.* **94,** 7588-7602.

Graham E. K., Schwab, J. A., Sopkin, S. M., and Takei, H. (1988) The pressure and temperature-dependence of the elastic properties of single-crystal fayalite Fe_2SiO_4. *Phys. Chem. Miner.* **16,** 186-198.

Greegor, R. B. and Lytle, F. W. (1983) Preliminary Investigation of Ti-Sit Geometry in Lunar Volcanic and Impact Glasses by X-Ray Absorption Spectroscopy. *Lunar Planet. Sci. Conf. Abstr. Book***, 14,** 257-258.

Greegor, R. B., Lytle, F.W., Sandstrom, D.R., Wong, J., and Schultz, P. (1983) Investigation of TiO_2-SiO_2 Glasses by X-Ray Absorption Spectroscopy. *Journal of Non-Crystalline Solids,* **55**, 27-43.

Greenwood, J.P., Itoh, S., Sakamoto, N., Warren, P., Taylor, L., and Yurimoto, H. (2011) Hydrogen isotope ratios in lunar rocks indicate delivery of cometary water to the Moon. *Nature Geoscience.,* **4,** 79-82.

Greenwood, J.P., Itoh, S., Sakamoto, N., Warren, P.H., Taylor, L.A., and Yurimoto, H. (2012) Towards a wetter Moon. Implications of high volatile abundances in lunar apatite. *Lunar and Planetary Science Conference XLIII.* Abstract # 2089.

Grove, T.L. and Krawczynski, M.J. (2009) Lunar mare volcanism: Where did the magmas come from? *Elements,* **5,** 29-34.

Hauri, E.H., Weinreich, T., Saal, A.E., Rutherford, M.C., and Van Orman, J.A. (2011) High Pre-Eruptive Water Contents Preserved in Lunar Melt Inclusions. *Science*, **333**, 213-215.

Hazen, R. M. (1997) Effects of temperature and pressure on crystal-structure of ferromagnesian olivine. *American Mineralogist.* **62,** 286-295.

Heiken, G. H., McKay, D. S., Anderson, D.H., and Butler, P. Jr. (1975) The source of sublimates on the Apollo 15 green and Apollo 17 orange glass samples. *Proc. Lunar Planet. Sci. Conf.*, **6**, 1673-1699.

Hess, P.C. (1991) Diapirism and the Origin of High TiO2 Mare Glasses. *Geophysical Research Letters*, **18,** No. 11, 2069-2072.

Hess, P.C. (2000) On the source regions for mare picrite glasses. *Journal of Geophysical Research*, **105**, No. E2, 44347-4360.

Hess, P.C. and Parmentier, E.M. (1993) Overturn of magma ocean ilmenite cumulate layer: Implications for lunar magmatic evolution and formation of a lunar core. *Proc. Lunar Planet Sci. Conf.,* **24,** 651-652.

Hugh-Jones D. (1997) Thermal expansion of $MgSiO_3$ and $FeSiO_3$ ortho- and clinopyroxenes. *American Mineralogist,* **82,** 689-696.

Hugh-Jones D. A. and Angel, R. J. (1994) A compressional study of $MgSiO_3$ orthoenstatite up to 8.5-GPa. *American Mineralogist,* **79,** 405-410.

Hugh-Jones D. A. and Angel, R. J. (1997) Effect of Ca^{2+} and Fe^{2+} on the equation of state of $MgSiO_3$ orthopyroxene. *J. Geophys. Res. Solid Earth,* **102**, 12333-12340.

Isaak D. G., Graham, E. K., Bass, J. D., and Wang, H. (1993) The elastic properties of single-crystal fayalite as determined by dynamical measurement techniques. *Pure Appl. Geophys.* **141,** 393-414.

Jacobs M. H. G. and de Jong, B. (2007) Placing constraints on phase equilibria and thermophysical properties in the system MgO-SiO_2 by a thermodynamically consistent vibrational method. *Geochim. Cosmochim. Acta,* **71,** 3630-3655.

Kennedy, G.C. and Higgins, G.H. (1975) A lunar core and the Moon's magnetic field. *The Moon,* **12,** 401-406.

Knoche, R. and Luth, R. W., (1996) Density measurements on melts at high pressure using the sink/float method: Limitations and possibilities. *Chemical Geology.* **128,** 229-243.

Krawczynski, M.J., and Grove, T.L. (2012) Experimental investigation of the influence of oxygen fugacity on the source depths for high titanium lunar ultramafic magmas. *Geochim. Cosmochim. Acta*, **79**, 1-19.

Lange, R.A. and Carmichael, ISE (1987) Densities of Na_2O-K_2O-CaO-MgO-FeO-Fe_2O_3-Al_2O_3-TiO_2-SiO_2 liquids: new measurements and derived partial molar properties. *Geochimica et Cosmochimica Acta,* **51**: 2931-2946.

Liu, Q. and Lange, R. A. (2001) The partial molar volume and thermal expansivity of TiO_2 in alkali silicate melts: Systematic variation with Ti Coordination. *Geochim. Cosmochim. Acta.***65**(14), 2379-2393.

Liu, W. and Li, B.S. (2006) Thermal equation of state of $(Mg_{0.9}Fe_{0.1})_2SiO_4$ olivine. *Phys. Earth Planet. Inter.* **157,** 188-195.

Longhi, J. (1980) A model of early lunar differentiation. *Proc. Lunar Planet. Sci. Conf,* **11,** 289-315.

McCubbin, F.M., Steele, A., Hauri, E.H., Nekvasil, H., Yamashita, S., and Hemley, R.J. (2010a) Nominally hydrous magmatism on the Moon. *Proc. Natl. Acad. Sci.*, **107**, 11223-11228.

McCubbin, F.M., Steele, A., Nekvasil, H., Schneiders, A., Rose, T., Fries, M., Carpenter, P.K., and Jolliff, B.L. (2010b) Detection of structurally bound hydroxyl from Apollo Mare basalt 15058,128 using TOF-SIMS. *American Mineralogist*, **95,** 1141-1150.

Murthy, V.R., Evenson, N.M., and Hall, H.T. (1971) Model of Early Lunar Differentiation. *Letters to Nature*, **234,** 267 & 290.

Mysen, B. O. (1987) Magmatic silicate melts: Relations between bulk composition, structure and properties. *Magmatic Processes: Physiochemical Principles,* © The Geochemical Society, Special Publication **No. 1.** 357-399.

Mysen, B. and Neuville, D. (1995) Effect of temperature and TiO2 content on the structure of $Na_2Si_2O_5$-$Na_2Ti_2O_5$ melts and glasses. *Geochim. Cosmochim. Act.* **59**(2), 325-342.

Ochs, F.A. and Lange, R.A. (1999) The density of hydrous magmatic liquids. *Science,* **283**, 1314-1317.

Rapp, J.F., and Draper, D.S. (2012) Experimental fractional crystallization of the lunar magma ocean. *Lunar and Planetary Science Conference XLIII.* Abstract # 2048.

Ridley, W. I., Reid, A.M., and Warner, J.L. (1973) Apollo 15 green glasses. *Phys. Earth Planet. Inter.,* **7**, 133-136.

Rutherford, M.J. and Papale, P. (2009) Origin of basalt fire-fountain eruptions on Earth versus the Moon. *Geology*, **37,** 219-222.

Saal, A.E., Hauri, E.H., Lo Cascio, M., Wan Orman, J.A., Rutherford, M.J., and Cooper, R.F. (2008) Volatile content of lunar volcanic glasses and the presence of water in the Moon's interior. *Nature,* **454,** 193-195.

Sandstrom, D.R., Lytle, F.W., Wei, P.S.P., Greegor, R.B., Wong, J., and Schultz, P. (1980) Coordination of Ti in TiO_2-SiO_2 Glass by X-Ray Absorption Spectroscopy. *Journal of Non-Crystalline Solids*, **41,** 201-207.

Sato, M. (1979) The driving mechanism of lunar pyroclastic eruptions inferred from the oxygen fugacity behavior of Apollo 17 orange glass. *Proc. Lunar Planet. Sci. Conf.,* **10**, 311-325.

Sharp, Z.D., McCubbin, F.M., and Shearer, C.K. (2012) A unifying theory for H-bearing volatiles on the Moon. *Lunar and Planetary Science Conference XLIII.* Abstract # 2751.

Shearer C. K., Hess, P.C., Wieczorek, M.A., Pritchard, M.E., Parmentier, E.M., Borg, L.E., Longhi, J., Elkins-Tanton, L.T., Neal, C.R., Antonenko, I., Canup, R.M., Halliday, A.N., Grove, T.L., Hager, B.H., Lee, D.C., and Wiechert, U. (2006) Thermal and Magmatic Evolution of the Moon. *Reviews in Mineralogy & Geochemistry*, **60**, 365-518.

Skinner B. J. (1956) Physical properties of end-members of the garnet group. *American Mineralogist.* **41,** 428-436.

Skinner B. J. (1966) Thermal expansion. In *Handbook of Physical Constants* (ed. S. P. Clark).

Smith, J.V., Anderson, A.T., Newton, R.C., Olsen, E.J., and Wyllie, P.J. (1970) A petrologic model for the Moon based on petrogenesis, experimental petrology, and physical properties. *The Journal of Geology*, **78,** 381-405.

Smith, J. R. and Agee, C. B. (1997) Compressibility of molten "green glass" and crystal-liquid density crossovers in low-Ti lunar magma. *Geochim. Cosmochim. Acta* **61,** 2139-2145.

Smyth, J. R. (1975) High temperature crystal-chemistry of fayalite. *American Mineralogist*, **60,** 1092-1097.

Snyder, G.A., Taylor, L.A., and Neal, C.R. (1992) A chemical model for generating the sources of mare basalts: Combined equilibrium and fractional crystallization of the lunar magmasphere. *Geochim. Cosmochim. Acta,* **56**, 3809-3823.

Stolper, E. M., Walker, D., Hager, B.H., Hays, J.F. (1981) Melt Segregation from Partially Molten Source Region: The Importance of Melt Density and Source Region Size. *J. Geophys. Res.* **86**, 6161-6271.

Sumino Y. and Anderson, O. L. (1984) Elastic constants of minerals. In CRC *Handbook of the Physical Properties of Rocks* (ed. S. Carmichael). CRC Press, Boca, Raton, FL.

Suzuki, I. (1975) Thermal expansion of periclase and olivine, and their anharmonic properties. *J. Phys. Earth* **23,** 145-159.

Suzuki, I., Seya, K., Takei, H., and Sumino, Y. (1981) Thermal-expansion of fayalite, Fe_2SiO_3. *Phys. Chem. Miner.* **7,** 60-6.

Suzuki, A., Ohtani, E., Kato, T. (1998) Density and thermal expansion of a peridotite melt at high pressure. *Phys. Earth Planet. Inter.* **107,** 53-61.

Toplis, M.J. (2005) The thermodynamics of iron and magnesium partitioning between olivine and liquid: criteria for assessing and predicting equilibrium in natural and experimental systems. *Contrib Mineral Petrol.* **149,** 22-39.

Ulmer, P (1989) The dependence of the Fe^{2+}- Mg cation-partitioning between olivine and basaltic liquid on pressure, temperature and composition. *Contrib Mineral Petrol.* **101,** 261-273.

Vander Kaaden, K.E., McCubbin, F.M., Whitson, E.S., Hauri, E.H., and J. Wang (2012) Partitioning of F, Cl, and H_2O Between Apatite and a Synthetic Shergottite Liquid (QUE 94201) at 1.0 GPa and 990-1000°C. *Lunar and Planetary Science Conference XLIII.* Abstract # 1247.

Van Kan Parker M., C. B. Agee, M. S. Duncan, and W. van Westrenen (2011) Compressibility of molten Apollo 17 orange glass and implications for density crossovers in the lunar mantle. *Geochim. Cosmochim. Acta*, **75**(4), 1161-1172.

Wagner, T.P. and Grove, T.L. (1997) Experimental constraints on the origin of lunar high-Ti ultramafic glasses. *Geochim. Cosmochim. Acta*, **61**(6), 1315-1327.

Warren, P.H. (1985) The magma ocean concept and lunar evolution. *Ann. Rev. Earth Planet. Sci.,* **13,** 201-240.

Warren, P. H. (1992) Inheritance of silicate differentiation during lunar origin by giant impact. *Earth and Planetary Science Letters,* **112,** 101-116.

Wieczorek, M.A., Jollif, B.L., Khan, A., Pritchard, M.E., Weiss, B.P., Williams, J.G., Hood, L.L., Righter, K., Neal, C.R., Shearer, C.K., McCallum, I.S., Tompkins, S., Hawke, B.R., Peterson, C., Gillis, J.J., and Busey, B. (2006) The constitution and structure of the lunar interior. *Reviews in Mineralogy & Geochemistry*, **60**, 221-364.

Williams, Q. and Jeanloz, R. (1998) Spectroscopic evidence for pressure-induced coordination changes in silicate glasses and melts, *Science*, **239,** 902-905.

Wood, J.A., Dickey, J.S. Jr., Marvin, U.B., and Powel, B.N. (1970) Lunar anorthosites and a geophysical model of the moon. *Proc of the Apollo 11 Lunar Sci. Conf.,* **1,** 965-988.

Zhang L., Ahsbahs, H., Kutoglu, A., and Geiger, C.A. (1999) Single-crystal hydrostatic compression of synthetic pyrope, almandine, spessartine, grossular, and andradite garnets at high pressures. *Phys. Chem. Miner.* **27,** 52-58.

Zhang, Y. (2011) “Water” in lunar basalts: The role of molecular hydrogen (H_2), especially in the diffusion of the H component. *Lunar and Planetary Science Conference XLII.* Abstract # 1957.